A Two-Dimensional Magneto-Optical Trap for a Strontium Clock

Andrew Whimster

München 2023

A Two-Dimensional Magneto-Optical Trap for a Strontium Clock

Masterarbeit an der Fakultät für Physik
Ludwig-Maximilians-Universität München

vorgelegt von

Andrew Whimster

aus High Wycombe, Großbritannien

München, den 1. Dezember 2023

Contents

List of Figures

Chapter 1

Introduction

Time plays such a ubiquitous role in human affairs that it is often taken for granted. Indeed, until Einstein developed the theory of relativity, time was seen as absolute and uniform throughout the universe. Yet from GPS measurements to high-speed global communications networks, the technology of the modern world is filled with technical challenges to accurately measure and synchronise time, often requiring relativistic corrections [1, 2]. Furthermore, the concept that observers in different frames might disagree as to the time at which certain events occurred is in profound opposition to quantum mechanics, in which the flow of time is universal for all observers and absolute, as in Newtonian physics.

Far from becoming less important, investigation into the nature of time is now central to many deep physical questions, not the least of which is how we are to reconcile relativistic and quantum theory [3]. A consistent theory of quantum gravity would have to resolve the problem of time, and perhaps make precise predictions which could only be made using instruments with a high degree of sensitivity to the passage of time. For these reasons, from technological challenges to fundamental physics, precise metrology and its continued development plays an important role in human society.

Our relationship with time has always been central to human culture and one closely related to the development of science and technology. Here a brief sketch of the history of time will be made, before turning to the increasing precision with which science measures and makes use of time, culminating in the modern optical lattice clock — the experiment we are here concerned with. After an overview of our planned experiment we will turn to the first small steps toward this goal — a two-dimensional magneto-optical trap that will be used to perform initial trapping of the Strontium atoms, and which is the focus of this thesis.

A Brief History of Time

"Time is what a clock measures."
– Albert Einstein

Throughout history we have measured the passage of time in days and years. The rhythm of night and day was our most immediate and reliable measure of time while the

seasons, passing in a yearly cycle, were far less regular. Between these two extremes the lunar month, of around 28 days, was found to provide an intermediate frequency with which to regulate our lives.

However, the length of a lunar month is difficult to define and measure precisely, and it was not until Julius Caesar established a solar calendar that time found firmer footing. Rather than relying upon ad hoc adjustments by astronomers, this solar year consisted of 365 days with a leap day every four years, with an error of 11 minutes every year. Accurate to a relative precision of $2\text{x}10^{-5}$, the Julian Calendar is not a purely Roman invention. Thousands of years of careful astronomical measurements were intercalated to determine the number of years between leap years, a system which was made more precise in the Gregorian calendar we use today, established in 1582 with a relative precision of $8\text{x}10^{-7}$.

By this time the Age of Exploration was well underway, and our needs had shifted from the absolute measure of months and seasons across hundreds of years, to the relative measurement of time on the order of the hours and days demanded for accurate navigation between continents. Magellan circumnavigated the globe using an hourglass, an imprecise measure who's period might vary by several parts in a hundred. However, it wasn't sailors, but Galileo Galilei who first designed, and Christiaan Huygens who first constructed, the pendulum clocks which provided for the navigational and scientific demands of their day, which measured time to a relative precision of around 10^{-4}. While the Gregorian calendar might be more precise than the pendulum clock, what was important was the ability to accurately sub-divide time into intervals relevant to navigation, which meant minutes and hours rather than days and months.

The development of clock technology advanced steadily, but it was not until the quartz-crystal clock was invented in 1928 that pendulum clocks were replaced as the most accurate timekeepers. In the 1950's atomic clocks were developed and in turn demonstrated higher precision than quartz-oscillators. We will give a brief overview of atomic clocks and their operation before discussing our experiment.

Atomic Clocks

"Never measure anything but frequency!"
— Arthur Schawlow

James Clerk Maxwell was the first to suggest using atoms themselves as a frequency source for a clock [4]. As all atoms of a given element are identical, a clock which defines it's cycle frequency upon an atomic transition should be the same for all observers. Although there are systematic considerations to bear in mind — the shifting of atomic transitions by black-body radiation is one of the most significant — these transitions do not vary, and a great deal of energy has been invested into the development of atomic

clocks in the past century [5].

Modern atomic clocks provide a frequency source by locking the frequency of a laser to the frequency of an atomic transition. The counting of cycles of time is inherently a digital process [6] and reduces sensitivity to a number of noise sources. Thus, physicists do their best to measure frequencies wherever they can, and these frequencies are in turn best resolved relative to a high precision frequency standard such as an atomic clock. Whether the object to be measured is the size of the proton [7], or the frequency of a gravitational wave [8], the precision and systematics of such a measurement will be conducted with reference to frequency space and the many methods available to characterise and improve measurements made in this way. The presence of a local frequency oscillator is often critical to high precision experiments.

The original atomic clock was a caesium clock, working in the microwave frequency [5], and the technology has since seen significant development and now operate as local oscillators in many experiments. Modern fountain clocks [9] launch caesium atoms vertically before they were addressed with resonant microwaves with a $\pi/2$-pulse of light, placing the atoms in a superposition state. As the caesium atom, under the influence of gravity, falls past the microwave source the atom is then once more struck with a $\pi/2$-pulse. In the case that the microwave is in perfect resonance with the atomic frequency, the atoms transition into a maximally excited state. If the microwave source is not on resonance, then the second pulse would be out of phase and the occupation probability of the atom would be less than one. By maximising the signal from excited atoms, it is possible to lock the maser to the caesium clock transition — the caesium transition is the "pendulum" of our clock. The microwave source itself is then the stable frequency source which, after correcting systematic variations caused by blackbody radiation and gravitational shifts, and other confounding factors, should be the same everywhere on Earth. To this day, the second is defined as the frequency of the hyperfine transition of the caesium ground state, and many labs have a caesium fountain clock as a local frequency source.

Today, optical lattice clocks are seen as the successors to the fountain clocks which are ubiquitous in precision laboratories. Their appeal is simple — optical frequencies have orders of magnitude higher frequencies and thus their relative precision is orders of magnitude better than maser technologies. The continued use of fountain clocks is partly historical, partly due to the great maturity of microwave technology. Indeed, the technology of microwave sources, or masers, is so well understood that optical lattice clocks are not used in isolation, but rather to entrain a local maser to the precise frequency of the optical lattice clock. However, in 2005 the optical frequency comb was invented [6, 10], and the optical lattice clock became a possibility.

The principles of lattice clocks are simple, even if their realisation is more complex. First, atoms are emitted, from an oven or dispenser, before being trapped and cooled using resonant lasers. This usually involves a sequence of magneto-optical traps, or MOTs,

which are used to cool and trap atoms. In Alkali-Earth atoms, several MOTs are used in turn to cool the atomic ensemble to nK temperatures. These are then loaded into a "*magic*" lattice [11], which consist of standing waves of lasers of a frequency chosen for having the same polarizability, and thus trapping force, for both the ground and excited states of the clock transition. This magic lattice allows the transition to be probed while experiencing a minimum of heating or motion. With great care and effort, such systems can measure time with higher precisions than the caesium clocks which define the second.

Analogous to the fountain clock, the clock laser is tuned to maximise the excitation probability of the atoms trapped in the lattice. Once a clock laser is on resonance with the atomic clock transition, an optical frequency comb is used to generate a beat frequency with a known wavelength [12]. This beat frequency is on the order of microwave transitions, to which a maser may be locked. Here we see the value of the mature maser technology, as once we have a maser entrained with an optical clock frequency, we can then "plug and play" all the rest of our timekeeping devices to this well understood piece of technology.

Experimental Outline

The aim of our experiment is to build a compact and efficient strontium lattice clock. Strontium atoms are heated to a vapour in an oven before being trapped, cooled to nK temperatures [13]. These cool atoms will then be loaded into a magic optical lattice, whereupon a clock laser will be brought into resonance with the clock transition of the cool Sr atoms. Here the lattice will be one-dimensional and, consequently, have a limited capacity of atoms it can trap.

In this thesis we will undertake the first step of our atomic clock — the construction of a compact two-dimensional MOT with which we will load subsequent MOTs for cooling and eventually the optical lattice of the clock proper. The precision of our clock relies upon large sample size and fast cycle times. Thus, the key figure of merit for our 2D MOT is a high atomic flux.

We will first survey the theory of MOTs, in particular examining the interaction of light and atoms as represented in a 2-level system. This will allow us to derive the behaviour of Rabi oscillations and from there the formalism of optical Bloch equations. This groundwork will allow us to discuss the specifics of MOTs and make some initial calculations for our design.

Next we will characterise our atomic sources, in this case a home-built oven and a commercial oven. After discussing the theory of these effusive cells and of absorption spectroscopy, we will characterise their behaviour and determine their suitability for the loading of our 2D MOT.

Design of the magnetic fields required for atomic trapping is the focus of the next chapter. After a brief overview of the theory of electromagnets and permanent magnets, we conduct a short literature review before simulating the magnetic fields we require for our 2D MOT. We then program and use a three-axis magnetic sensor rig to characterise the magnetic fields induced by our set up and ensure that our MOT chamber and magnetic arrangements are suitable.

In the penultimate chapter, we discuss the assembly and trapping of the MOT, including the design and assembly of compact beam launchers for our cooling beams, before characterising the performance of our MOT.

We conclude with an overview of the thesis and an outlook on future steps for our optical lattice clock.

Chapter 2

Two-Dimensional Magneto-Optical Trap: Theory and Design

Magneto-Optical Traps rely upon the interaction of coherent laser light, with the aid of magnetic fields, to trap atoms in free space [14]. The design of a magneto-optical trap (MOT) must ensure that this interaction of light with the atoms is tuned to the needs of our experiment. As discussed in the previous chapter, we will be building a 2D MOT in order to provide a high flux of Sr atoms in order to load a 3D MOT which will cool atoms for our optical lattice clock. Thus, our 2D MOT is tasked with providing as high flux of atoms as possible — the more atoms per second the 2D MOT can provide, the faster we can load a large ensemble of atoms into our clock per cycle time and thus the higher the precision with which we can measure the clock frequency of Sr.

This chapter will begin with a discussion of the semi-classical approach to the light-atom interaction. We will discuss Rabi oscillations and the use of density matrices to understand the behaviour of our atoms under incoherent processes such as spontaneous decay [15]. Armed with this knowledge we will then consider the phenomena of Doppler Cooling and Magneto-Optico traps in general, before discussing the specifics of working with strontium and the design considerations of our own 2D MOT.

2.1 Theory of Magneto-Optical Traps

2.1.1 Semi-classical approach to light-atom interaction

To understand the operation of a Magneto-Optical Trap we need to understand how atoms interact with laser-light. Beginning with an atom represented as a simple 2-level system, we will introduce near-resonant light and see how this induces Rabi oscillations in the atom. This simplified view will be expanded to mixed states with density matrices which allows us to develop the Bloch vector formalism. This conceptual framework allows us to describe the dynamics of laser cooling and trapping in our MOT.

We consider a transition between two states of an atom. If the transition is driven by near-resonant light which has negligible coupling to other states, we can approximate this as a two-level system

$$|\Psi(t)\rangle = c_g(t)e^{-i\frac{E_g}{\hbar}t}|g\rangle + c_e(t)e^{-i\frac{E_e}{\hbar}t}|e\rangle \tag{2.1}$$

where c_g is the probability amplitude of the gronud state and c_e is the probability amplitude of our excited state. We define the transition frequency as determined by the energy difference between the ground and excited states

$$E_e - E_g = \hbar\omega_0, \tag{2.2}$$

from which the interaction-free Hamiltonian may be described as

$$\hat{H}_0 = \hbar \begin{pmatrix} 0 & 0 \\ 0 & \omega_0 \end{pmatrix}. \tag{2.3}$$

The ground level atom is defined to be at zero energy with the excited state having energy ω_0, with no coherence between the two. The atom is coupled to a near-resonant laser:

$$\boldsymbol{E}(\boldsymbol{r_0}, t) = \boldsymbol{E}(\boldsymbol{r_0}) \cos(\omega_L t + \phi(\boldsymbol{r_0})) \tag{2.4}$$

where $\boldsymbol{E}(\boldsymbol{r_0}, t)$ describes the electric field as a function of position and time, ω_L is the laser frequency and $\phi(\boldsymbol{r_0}$ is a phase-shift of the electric field as a function of position. This interaction may be describe with the interaction Hamiltonian as the light field interacts with the electric dipole of the atom:

$$\hat{H}_I(t) = -\hat{D}\boldsymbol{E}(\boldsymbol{r}_0, t) \tag{2.5}$$

which couples the ground and excited states. The transition matrix elements of the Hamiltonian may be denoted:

$$W_{ki} = -\langle k|\hat{D}\boldsymbol{\epsilon}|i\rangle \boldsymbol{E}(\boldsymbol{r}_0) = -dE(\boldsymbol{r}_0) \tag{2.6}$$

where $\boldsymbol{\epsilon}$ is the polarization of our light and d is the matrix element of $\hat{D}$ projected onto the polarization of the light, from which we may define the *Rabi frequency*:

$$\Omega_0 = \frac{W_{ki}}{\hbar}. \tag{2.7}$$

Thus we may describe the entire Hamiltonian:

$$\hat{H} = \hat{H}_0 + \hat{H}_I = \hbar \begin{pmatrix} 0 & \Omega_0 \cos(\omega_L t + \phi(\boldsymbol{r_0})) \\ \Omega_0 \cos(\omega_L t + \phi(\boldsymbol{r_0})) & \omega_0. \end{pmatrix} \tag{2.8}$$

We now make a series of assumptions which will allow us to solve the Schrödinger Equation that describes this system, understand the phenomena of Rabi oscillations and lead us in an intuitive way towards the Bloch vector formalism:

1. The wavelength of our light is long enough that the EM field is constant across the volume of our atom, the so-called *Long Wavelength Approximation*, i.e. $\phi(\boldsymbol{r_0}) = \phi$,
2. As ϕ is simply a global phase, it may be absorbed into the phase difference between

the ground and excited states, known as the *Rotating Frame of the Atom*,

$$|\Psi(t)\rangle = c_g(t)|g\rangle + c_e(t)e^{-i\omega_0 t}|e\rangle, \tag{2.9}$$

3. The condition of resonant laser-light is relaxed, introducing the notion of a detuning $\delta = \omega_0 - \omega_L$,
4. The above condition is used to expand our basis in the *Rotating Frame of Light*, which simplifies the expression of the dynamics of coherence and detuning between atom and light frames:

$$|\Psi(t)\rangle = c_g(t)|g\rangle + c_e(t)e^{-i\omega_0 t}|e\rangle = \tilde{c}_g(t)|g\rangle + \tilde{c}_e(t)e^{-i\delta t}|e\rangle \tag{2.10}$$

with these simplifications, we may now describe our system with the Hamiltonian

$$\hat{H} = \frac{\hbar}{2}\begin{pmatrix} -\delta & \Omega_0 \\ \Omega_0 & +\delta \end{pmatrix}, \tag{2.11}$$

and, applying Schrödinger's equation, describe our state amplitudes for zero detuning, i.e. $\delta = 0$, as a function of time

$$\frac{d}{dt}\tilde{c}_g(t) = \frac{i}{2}\Omega_0\tilde{c}_e(t), \tag{2.12a}$$

$$\frac{d}{dt}\tilde{c}_e(t) = \frac{i}{2}\Omega_0\tilde{c}_g(t). \tag{2.12b}$$

Taking the time derivative of the second equation and plugging into the first, we see that our system exhibits harmonic oscillations at the Rabi frequency:

$$\frac{d^2}{dt^2}\tilde{c}_e(t) = -\frac{\Omega_0^2}{2}\tilde{c}_e(t), \tag{2.13}$$

where the probability of finding our atom in the excited state is

$$P_e(t) = |c_e(t)|^2, \tag{2.14}$$

i.e. we see Rabi flopping of the occupation probability of the excited and ground states between 1 and 0. In the detuned case, the effective Rabi frequency is increased

$$\Omega_{\text{eff}} = \sqrt{\Omega_0^2 + \delta^2}, \tag{2.15}$$

while the maximal probability of occupation of the excited state is reduced to

$$|c_e^{\max}|^2 = \frac{\Omega_0^2}{\Omega_{eff}^2}. \tag{2.16}$$

Rabi flopping underlies almost all interactions between light and atoms that we are

concerned with in MOTs. However, the picture of an idealised pure state does not allow us to describe incoherent phenomenon such as spontaneous emission. To understand such behaviour, we introduce the density matrix formalism, in which our state is described as

$$\hat{\rho} = \begin{pmatrix} |c_g|^2 & |c_g||c_e|e^{-i\phi} \\ |c_g||c_e|e^{i\phi} & |c_e|^2 \end{pmatrix} = \begin{pmatrix} \rho_{11} & \rho_{12} \\ \rho_{21} & \rho_{22} \end{pmatrix} \tag{2.17}$$

where the diagonal elements describe our populations and the off-diagonal terms describe our coherences. Proceeding analogously to our treatment of the pure system, we first consider the time evolution of ρ_{11}

$$\dot{\rho}_{11} = \frac{d}{dt}(c_g c_g^*) = \dot{c}_g c_g^* + c_g \dot{c_g}^*, \tag{2.18a}$$

$$= i\frac{\Omega_0}{2}(e^{i\delta t}\rho_{21} - e^{-i\delta t}\rho_{12}), \tag{2.18b}$$

repeating the same for our other terms, and returning to the rotating light frame

$$\dot{\rho}_{11} = i\frac{\Omega_0}{2}(\tilde{\rho_{21}} - \tilde{\rho_{12}}), \tag{2.19a}$$

$$\dot{\rho}_{22} = i\frac{\Omega_0}{2}(\tilde{\rho_{12}} - \tilde{\rho_{21}}), \tag{2.19b}$$

$$\dot{\tilde{\rho}}_{12} = i\frac{\Omega_0}{2}(\rho_{22} - \rho_{11}) - i\delta\tilde{\rho}_{12}. \tag{2.19c}$$

However, as atomic transitions have a finite line-width, they also have a finite lifetime. Thus there is a non-zero probability of an atom in an excited state to spontaneously emit a photon as it drops to the ground state, and our equations must account for this. Here we will add this process to the equations *ad hoc*

$$\dot{\rho}_{11} = i\frac{\Omega_0}{2}(\tilde{\rho_{21}} - \tilde{\rho_{12}}) + \gamma\rho_{22}, \tag{2.20a}$$

$$\dot{\rho}_{22} = i\frac{\Omega_0}{2}(\tilde{\rho_{12}} - \tilde{\rho_{21}}) - \gamma\rho_{22}, \tag{2.20b}$$

$$\dot{\tilde{\rho}}_{12} = i\frac{\Omega_0}{2}(\rho_{22} - \rho_{11}) - (\frac{\gamma}{2} + i\delta\tilde{\rho}_{12}), \tag{2.20c}$$

where γ is our rate of spontaneous decay. These are the *damped optical Bloch equations*. In the steady-state, we expect the excited population to be:

$$\rho_{22} = \frac{s/2}{1 + s + 4\delta^2/\gamma^2} \tag{2.21}$$

where we define our saturation parameter as $s = I/I_0$ where I is our laser intensity and I the saturation intensity of the atom. From the above we expect photons to be scattered at the rate:

$$\Gamma_{ph} = \gamma\rho_{22} = \frac{\gamma}{2}\frac{s}{1 + s + 4\delta^2/\gamma^2} \tag{2.22}$$

This scattering rate is key to the process of laser cooling [16]. Seen as a whole, the scattering rate describes the absorption of a photon by our atom followed by it's re-emission. Thus, we expect to see that the atom absorbs the momentum of the photon, i.e. in the direction of propagation of laser light, and re-emits this photon for a net zero change in velocity. This results in a force acting upon our atom

$$\boldsymbol{F} = \hbar \boldsymbol{k} \Gamma_{ph} \tag{2.23}$$

where $\boldsymbol{k}$ is the wave-vector of our laser-light. It is this process that underlies the process of Doppler cooling and, by extension, Magneto-Optical Trapping.

2.1.2 Doppler Cooling and Optical Molasses

We may use this force to slow atoms. If we consider an atom moving through a counter-propagating, resonant light-field, we expect the atom to absorb photons with momentum opposite to the atom's current velocity and re-emit in a random direction. Both processes see a momentum "kick" imparted to the atom, but only the first has a net statistical result [17]. However, in order for this to occur, the laser-light must be resonant. If the atom is moving towards the laser then the light will be blue shifted in the atomic frame. Thus, in order to ensure a high scattering rate, the laser must be red-detuned in order to resonate in the atom's frame. This phenomena of optical Doppler shifting allows us to address certain sections of the velocity distribution of our atomic ensemble - this is known as Doppler cooling.

The Doppler shift is the frequency shift induced in light within the rest frame of the object in question, here the atom, and is defined as

$$\delta_D = \boldsymbol{k}\boldsymbol{v}, \tag{2.24}$$

where $\boldsymbol{v}$ is the velocity of the atom.

If we consider, in the 1D case, an ensemble of atoms with a broad velocity distribution, then by addressing both directions with a suitably red-detuned laser it is possible to compress the velocity distribution. An atom with a non-zero velocity is by definition moving toward one of the cooling lasers. Detuning of the laser-light allows us to cool the atoms, as their velocity moves them into resonance with the opposing laser.

Cooling can be extended to two or three dimensions with the simple addition of orthogonal laser in the other directions. When extended in this way we form an *Optical Molasses*.[14] The photon pressure of Optical Molasses can be seen as a frictive force opposing the motion of the atoms

$$\boldsymbol{F} = -\beta \boldsymbol{v}, \tag{2.25}$$

where

$$\beta = \frac{8\hbar k^2 \delta s \boldsymbol{v}}{\gamma(1+s+(2\delta/\gamma)^2)^2}. \tag{2.26}$$

However, this cooling effect has a limit, caused by the heating that occurs as the cooling light is re-emitted

$$T_D = \hbar\gamma/(2k_B), \tag{2.27}$$

known as the Doppler temperature.

As the Doppler temperature is proportional to the scattering rate, our blue optical transition, with a scattering rate of 30 MHz, will only be used as the first stage of cooling, while the red cooling transition with a scattering rate of 7.4 kHz is used to cool atoms in the 3D MOT [18]. For now, however, we are focussed on trapping atoms within a 2D MOT before transferring the atoms to the 3D blue MOT for first stage cooling. In this case, the fast scattering rate allows us to rapidly slow and capture our atoms.

This leaves us a final challenge to tackle: without some way to spatially confine the atoms, the atoms will diffuse throughout the system at the Doppler temperature. This spatial confinement is the next aspect of the MOT to be discussed.

2.1.3 Spatial Confinement with Magneto-Optical Trapping

In order to spatially trap our atoms, and counteract the diffusion caused by the Doppler temperature, we need to induce a shift in transition frequency as a function of position, just as the Doppler shift induces a shift as a function of velocity. To this end, a magnetic field gradient can be used to induce a Zeeman shift in the magnetic states of our atoms and tune the resonance profile of our ensemble to achieve spatial confinement.

To do this we need two things:

1. A Zeeman shift which increases with distance from our trap centre, and brings our atoms into resonance with our red-detuned lasers.
2. A method of ensuring that only laser light which gives a restoring force is resonant with our atoms.

In the 1D case, a magnetic field gradient with a zero-crossing at the trap centre gives us the correct resonance profile, as can be seen in Fig. 2.1. The zero-crossing marks a transition between the positive or negative Zeeman sub-states having their energies reduced by the Zeeman shift. This brings negative Zeeman sub-states into resonance with our red-detuned laser in the positive field and vice versa. Atoms which lie outside the trap centre are now selectively tuned to resonance with the quantization axis of their magnetic moment aligned along the magnetic field gradient. Our transitions entail a change in angular momentum, so circularly polarized light is required in order to conserve angular

momentum. By using circularly polarized light we can impart a spatially trapping force to the atoms, mediated by our magnetic fields.

The force of the laser on the atoms can be expanded to include the Zeeman shift δ_z

$$\delta_z = \frac{\mu' B}{\hbar}, \tag{2.28}$$

where μ' is the change in the magnetic moment due to the transition and B is the magnetic field, which gives us a total force equation

$$\boldsymbol{F} = -\beta \boldsymbol{v} - \kappa \boldsymbol{r}, \tag{2.29}$$

where

$$\kappa = \frac{\mu' b}{\hbar k}\beta, \tag{2.30}$$

where b is our magnetic field gradient.

The motion of atoms within our trap can be described using the explicit force equation:

$$\boldsymbol{F}_{\pm} = \pm \frac{\hbar \boldsymbol{k} \gamma}{2} \frac{a}{1 + a + (2\delta_{\pm}/\gamma)^2} \tag{2.31}$$

where

$$\delta_{\pm} = \delta_0 \mp \boldsymbol{k}\boldsymbol{v} \pm \frac{\mu' B}{\hbar}, \tag{2.32}$$

which will be central to calculating the motion of our atoms in later simulations.

2.2 Magneto-Optical Trap Calculations

2.2.1 Strontium

One outstanding feature of strontium's physical properties is its extremely narrow-linewidth ${}^1S_0 \leftrightarrow {}^3P_0$ clock transition, as show in Fig. 2.2. However, before the atom can be probed by such a narrow transition, it must be cooled and trapped in an optical lattice. In most labs, an oven containing Strontium is heated and slowed using a Zeeman slower before being trapped in a blue MOT. This blue MOT uses the high scattering rate of the ${}^1S_0 \leftrightarrow {}^1P_1$ transition in order to trap and cool the atom. As mentioned earlier, a high scattering rate also means a high Doppler temperature, thus once strontium is cooled by blue MOT light it is cooled in turn by red MOT light. The lower scattering rate of this transition makes it less amenable to trapping fast atoms, but it allows cooling to a much lower Doppler temperature before the atoms are loaded into an optical lattice. This lower temperature in turn entails a more precise measurement of our all-important clock transition.

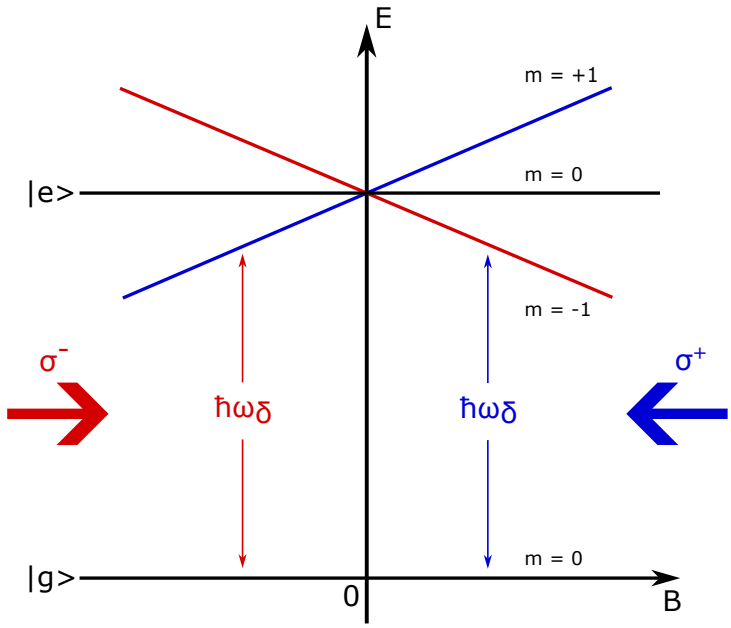

Figure 2.1 Position selective addressing of atoms using the Zeeman shift induced by a magnetic field and rotationally-polarized light.

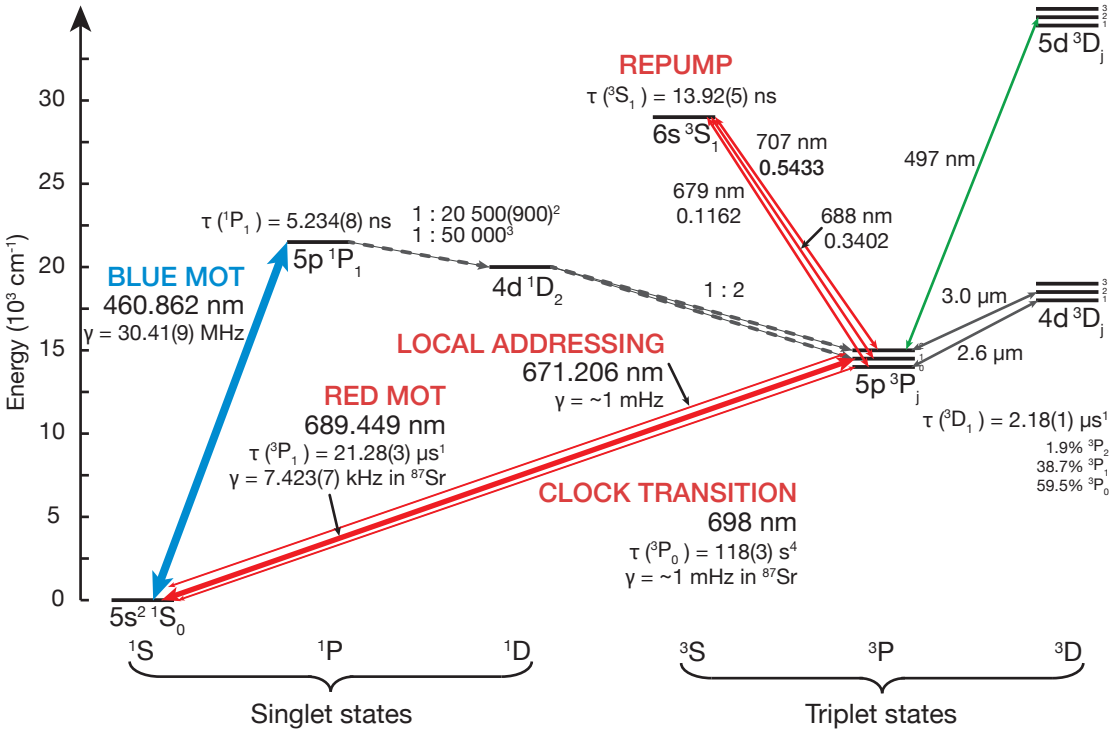

Figure 2.2 Strontium level scheme [19]. Our 2D MOT addresses the blue MOT transition.

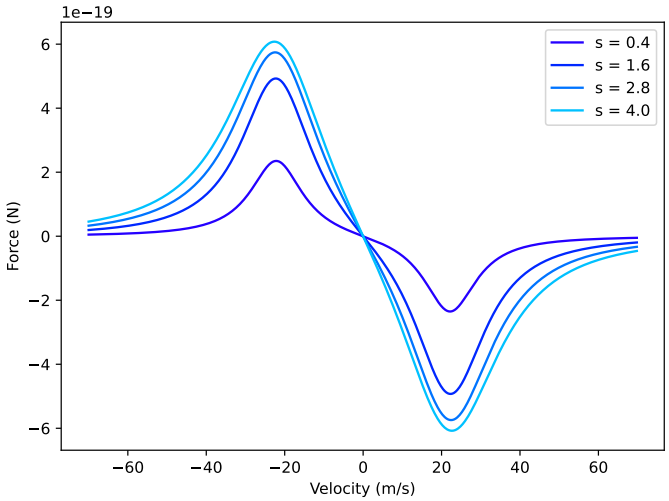

Figure 2.3 Force-Velocity curves for different values of laser intensity expressed in terms of the laser intensity at a detuning of -1.6 γ. The saturation values are linearly spaced, revealing saturation of the laser force around values of s = 3.

In our case, we would like to build a more compact realization for our atomic lattice clock and avoid a Zeeman slower altogether. In the absence of a Zeeman slower we will use a 2D MOT in order to trap atoms directly from the oven, using the atomic flux generated by this 2D MOT in order to load our 3D blue MOT. As we will discuss in later chapters, at the temperatures that are required to vapourize Sr, the atoms are moving with a mean velocity of around 400 m/s. In fact, most of the atoms emitted by our oven will be moving too fast to be trapped. We will overcome this limitation - one imposed by the lack of a Zeeman slower - by taking advantage of the compact setup that we plan to build. By moving the effusive nozzle of the oven as close as possible to the trapping region of the MOT, we will capture a far larger solid angle of the atomic beam and thus increase the loading efficiency of our MOT.

2.2.2 Force in a 2D MOT

The dispersion relation of our cooling laser upon a strontium atom can be plotted for a variety of saturation strengths using Eq. 2.31. As can be seen in Fig. 2.3, a negative detuning of - 1.6 γ can be expected to compress the velocity distribution of an atomic ensemble toward a mean velocity of zero, with peak deceleration occuring at 20 m/s. The saturation values are linearly spaced and display the saturation of the frictive force at around 3 s.

A shift in the detuning can be see in Fig 2.4 where the force is plotted for both blue- and red-detuned cases. Larger detunings increase the maximum velocity addressable by

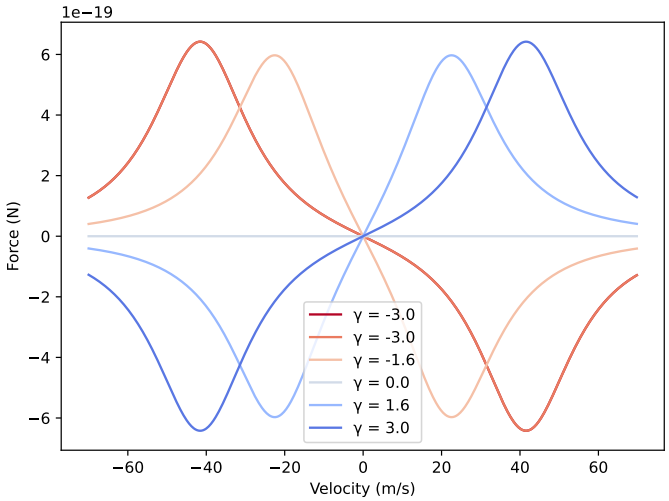

Figure 2.4 Force-velocity curves for different laser detunings (expressed in line-widths, γ) we can see that increasing the detuning allows us to address a broader distribution of atoms, but reduces the trapping force at lower velocities. This reduces the trapping potential and thus the temperature of trapped atoms.

cooling lasers and reduces the trapping potential at low velocities. This would reduce the trap frequency and thus the trap temperature, which would improve the collimation of the atoms as they are emitted from the 2D MOT. However, care must be taken that the potential gradient the atoms cross is sufficient to slow them down — too large a detuning will address high velocity for times too short to trap them in the MOT [13].

We now introduce magnetic fields in order to trap the atoms. Setting the detuning to - 1.6 γ and saturation to 3s, the same dispersion curves may be plotted for different magnetic field gradients, as seen in Figs. 2.5,2.6. Unlike changes to the detuning, variation of the magnetic field gradient does not influence the force-velocity curves, rather translating them against the velocity further from the trap centre.

Comparing these two variables, it can be seen that a larger magnetic field gradient allows us to slow faster atoms at the trap boundary without changing other factors. On the other hand, a larger detuning allows us to trap faster atoms and reduce trap temperature. With these distinctions in mind, we can plot the force as a scalar field as a function of force and velocity for the above trapping variables, as can be seen in Fig. 2.7

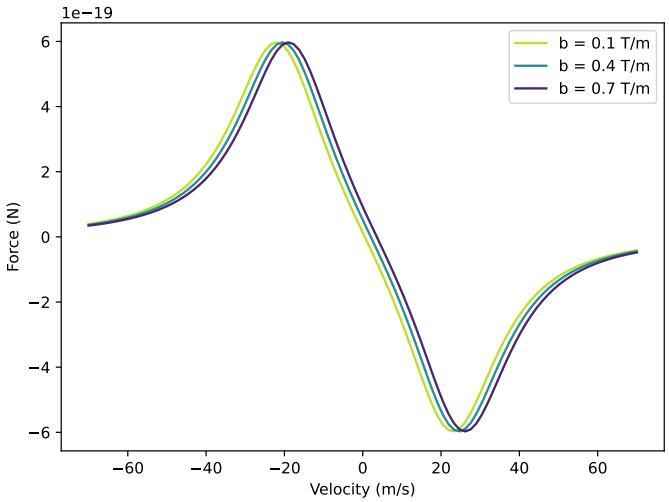

Figure 2.5 Force-Velocity curves for several different magnetic field gradients 0.5 mm from the trap centre. At the trap centre these curves overlap, as we would expect at the null-point of the field.

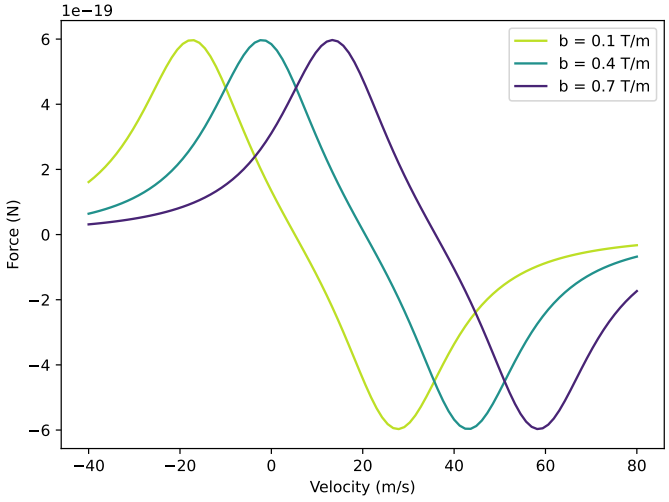

Figure 2.6 Force-Velocity curves for several different magnetic field gradients 5 mm before trap centre. Here the field gradients manifest in a shift of the addressed velocities.

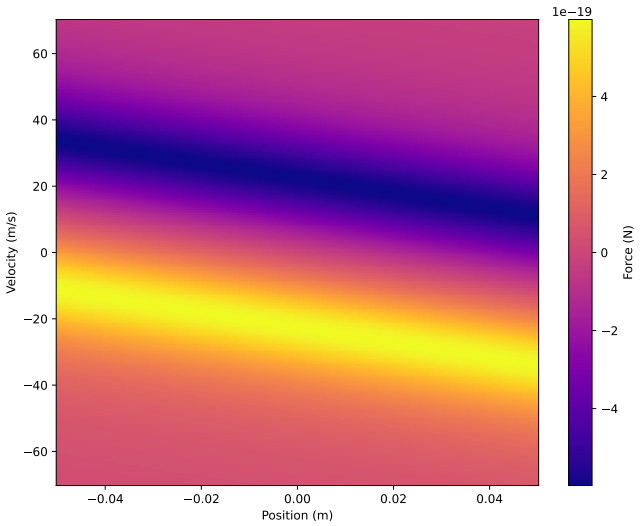

Figure 2.7 Force plotted as a function of temperature and velocity. It can be seen how the 2D MOT provides a "channel" down which the atoms are guided toward the centre of the MOT.

Chapter 3

Oven Characterisation

The oven provides atoms for the 2D MOT which traps them. Both components must perform to a high standard to ensure our clock has the fast loading rates it needs. We will also discuss some of the challenges that the ovens have provided during the course of this thesis.

In this chapter, we perform absorption spectroscopy on 2 ovens, one home-built and the other commercial. An understanding of the atomic flux as a function of oven temperature and angle, along with the velocity distribution of atoms in the atomic beam, will allow us to understand how best to operate the oven for highest trapping rate, and thus, highest precision for our atomic clock.

3.1 Oven Theory

The trapping rate of our 2D MOT is dependent upon the atomic flux through the trapping region and the velocity distribution of the atoms that pass through it. The first is a function of the angular distribution while the second can be understood from the perspective of Maxwell-Boltzmann statistics. In order to characterise these distributions for our two available sources we will perform absorption spectroscopy using the blue MOT transition, as its high scattering rate will give us greatest sensitivity to the atomic beam.

Here we will begin with a description of the velocity distribution of atomic beams before turning to the more complex angular distribution. The method of absorption spectroscopy will be discussed before we outline our implementation and results.

3.1.1 Velocity Distribution of Atomic Beams

We can model an oven as a volume containing a number of source atoms whose behaviour can be described using the ideal gas law:

$$pV = Nk_bT \tag{3.1}$$

where p is the pressure, V is the volume, N is the number of atoms, k_B is Boltzmann's constant and T is the temperature of the volume.

The velocities of the source atoms obey a Maxwell-Boltzmann distribution [20]:

$$\frac{dN}{dv} = NF(v) = \frac{4N}{\sqrt{\pi}}\frac{1}{\alpha^3}v^2 exp(-v^2/\alpha^2) \tag{3.2}$$

where $\alpha = \sqrt{\frac{2k_BT}{m}}$. Plotted for a variety of temperatures as the dotted lines in Fig. 3.1, we see that our mean velocity is around 400 m/s, significantly larger than our intended trapping speeds of around 50 m/s. This strengthens our motivation for bringing our oven as close to the MOT trapping centre, as discussed in the previous section. With such a small fraction of trappable atoms without the use of the Zeeman slower, we must ensure that a majority of those few atoms that move slow enough for us to trap pass through the trapping region. This will be examined more closely in the discussion of angular distribution

If we now place an aperture in our volume from which the atoms may effuse, the velocity distribution of the beam is modified by a factor of v; as the particles increase in velocity their probability of exiting the volume increases. From this, we may define the intensity of our atomic beam as a function of velocity as:

$$I(v) = \frac{2I_0}{\alpha^4}v^3 exp(-v^2/\alpha^2) \tag{3.3}$$

under the assumption that the mean free path λ_{MF} is much greater than the radius of the aperture w, although in practise $w \sim \lambda_{MF}$ is sufficient. This expression is known as the modified Maxwell-Boltzmann distribution. We can thus determine the velocity distribution of Strontium atoms within our oven chamber, and the distribution of those same atoms as they are emitted from the oven. As mentioned above, we plan to trap only atoms moving less than 100 m/s; as we can see from the detail in Fig. 3.1, changes in temperature make a negligible difference to the number of trappable atoms, due to the cubic rather than quadratic relationship of I with respect to v. This implies, dependent upon the angular distribution's reliance on temperature, that a hotter oven will provide more trappable atoms without a significant change in the velocity distribution. This is somewhat surprising, as one might intuitively assume that a hotter oven would reduce the fraction of trappable atoms.

We now have a sense of how the temperature of our oven influences the velocity distribution of our atoms, both inside the oven and those emitted by it. Next, the atomic flux as a function of their angle of emission will be discussed.

3.1.2 Angular Distribution of Atomic Beams

While the velocity distribution has a strong influence on the number of trappable atoms, we see that we have little opportunity to effect these numbers in a meaningful way. In

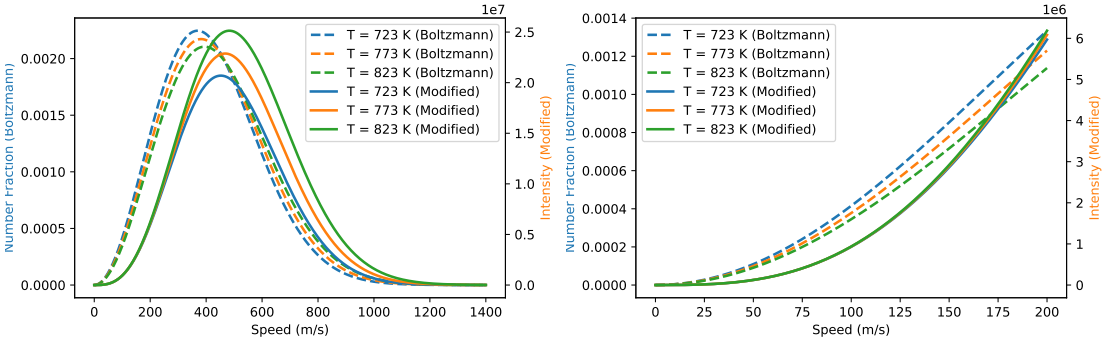

(a) Full Velocity Distributions **(b)** Velocity Distribution Detail

Figure 3.1 Maxwell-Boltzmann and Modified Maxwell-Boltzmann distributions for Strontium atoms in our oven. Note that in the detail in (b), changes to temperature have a negligible effect on the number of atoms we can trap.

contrast, the atomic flux as a function of its angular distribution of emission from the oven is much more sensitive to our control. The size and position of our trapping region are heavily influenced by the geometry of our setup, the laser optics used for the cooling beams and the magnetic fields we use. As such, we will spend some time determining not only how the angular distribution of our atoms may be derived, but also how we may use these equations to increase the amount of information we may extract from our absorption spectroscopy.

Two factors drive the angular distribution of our atomic beam: collisions with the vessel's walls – which influence the atoms through geometrical considerations – and interatomic collisions – which bring fluid dynamics into consideration. The first factor, atomic collisions with the walls, is a geometric consideration and drives the behaviour of our atoms when they rarely collide with one another. In this regime, they can be modelled as flowing through a vacuum in what is called *molecular flow*. However, as we increase the density of our atoms the second important factor, collisions between atoms, becomes more important and we move toward the *continuum regime*. In the continuum regime, Navier-Stokes equations must be used to model the gas as a fluid which begins to display hydrodynamic properties such as viscosity and turbulence. The Knudsen parameter is used to determine which regime we are in:

$$\mathrm{Kn} = \frac{\lambda_{MF}}{L} = \frac{k_B T}{\pi\sqrt{2}\sigma^2 p L} \tag{3.4}$$

where σ is the scattering cross section of Strontium, L is the length of the tube the atoms flow through and p is the vapour pressure of Strontium. For the case $\mathrm{Kn} \gg 1$ we are in the molecular flow regime, while $\mathrm{Kn} \ll 1$ is described by the continuum regime. In the current case $\mathrm{Kn} \sim 1$ and our atoms exhibit the behaviour of the intermediate regime.

From this model we would like to understand the atomic flux and angular distribution of our atomic beam. The theory we develop here will allow us to better interpret the data taken by absorption spectroscopy and thus model the angular distribution of our atomic flux. We will begin from the simple collision-free case exhibited in molecular flow before examining the more complex intermediate case which exhibits particle collisions.

The central mechanism governing atomic collisions with vessel walls is the law of diffuse reflection or Lambert's cosine law. On the atomic scale, all surfaces exhibit a high degree of roughness; by assuming that this causes atoms to be reflected from a given surface in all directions with equal probability, we can show that the angle from which we view such a surface determines the number of atoms that approach us. This is due to the fact that as we view a surface from the normal, the angle subtended by a unit area is at a maximum. As the viewing angle moves away from the normal, the solid angle subtended by a unit area is reduced as a function of $cos(\theta)$.

In the simple case of an aperture in a thin-wall, Knudsen showed that we expect the angular distribution to be described $j(\theta) = cos(\theta)$. However, later analysis by Clausing [21] showed that the use of a capillary of finite length can further collimate the beam, where $\beta = \frac{2r^2}{L}$ describes the geometric parameter which influences this collimation.[22] If we consider such a capillary from the perspective of Lambert's cosine law, any collision with the capillary wall is just as likely to scatter forward as backward. Thus, as collisions with the capillary wall increase, the probability that an atom will emerge from the capillary decreases. As the capillary becomes longer and/or more narrow, the angle through which an atom is likely to make its way through the capillary becomes increasingly small, which in turn constricts the angular distribution of atoms which emerge from the capillary. Thus a long, thin capillary increases atomic beam collimation and, as such, many modern atomic sources use arrays of micro-capillaries to maximise β and significantly tighten the angular distribution of atoms.

Both the transmission probability K and the angular distribution $j(\theta)$ are dependent only upon γ and are determined by the collision rate on the tube walls which may be approximated using:

$$\nu(x)/\nu_s = \zeta_1 - (\zeta_1 - \zeta_0)x \tag{3.5}$$

where ζ_1 and ζ_0 are the wall collision rates at entrance and exit of the tube, respectively.

3.1.3 Absorption Spectroscopy

Absorption spectroscopy uses the absorption and re-emission of resonant laser light to probe an atomic cloud for properties such as atomic flux and velocity distribution. By scanning the frequency of the laser the full velocity ensemble of the cloud is probed and, by integrating under the curve of the spectrum, the atomic flux of atoms through the laser is deduced.

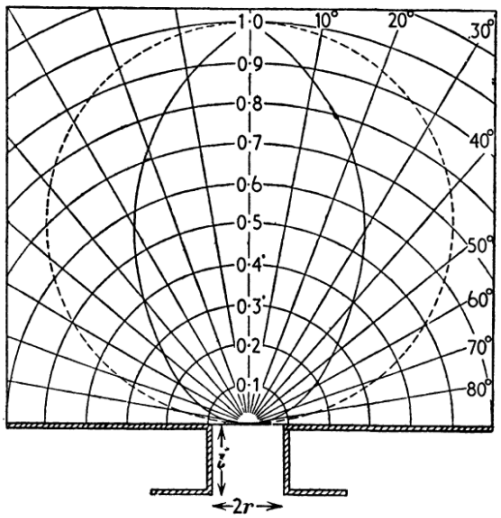

Figure 3.2 Dotted line shows cosine distribution shown by Knudsen for thin-walled apertures, while the solid line represents the distribution of a tube of length l derived by Clausius. Adapted from [20, 23]

The central mechanism is understood thanks once again to Lambert, in this case the Lambert-Beer Law:

$$I = I_0 e^{-OD(\delta)} \tag{3.6}$$

where I is the intensity of our laser light at a given point, I_o is the initial intensity of the laser and $OD(\delta)$ is the optical depth of our sample as a function of δ the detuning of the laser from resonance. The optical depth describes the amount of radiant power absorbed by a medium and is defined [24] in this case as:

$$OD = \int_0^l \sigma(\delta, x) n(x) dx \tag{3.7}$$

where l is the length of the chord of out atomic beam our laser traverses, σ is the scattering cross-section and n is the number density of our atomic cloud at x. The scattering cross-section is defined in turn as:

$$\sigma(\delta) = \frac{\sigma_0}{1 + \frac{4}{\gamma^2}(\delta + \delta_d)^2} \tag{3.8}$$

where σ_0 is the resonant scattering cross-section:

$$\sigma_0 = \frac{3\lambda_0^2}{2\pi} \tag{3.9}$$

for the the $\lambda_0 = 461$ nm cooling transition, γ is the scattering rate of this transition and

δ, δ_d are the laser detuning and the Doppler shift respectively.

The atoms leave the aperture with an angular distribution as discussed above and move outward in a cone assumed to be rotationally symmetric about the forward (z) axis. The Doppler shift δ_d is determined by the transverse component of the atomic velocity, from which the temperature of the atoms may be inferred.

3.2 Absorption Spectroscopy of the Ovens

3.2.1 Oven Spectroscopy Setup

Two ovens were tested using our absorption spectroscopy setup. One is a home-built oven, constructed by Etienne Staub and Eva Casotti [25, 26], the other a commercial oven designed and built by Createc Fischer GmbH. Although details of construction and control vary, the basic design of both ovens are the same. A crucible containing Strontium is connected to a nozzle built of micro-capillaries. Both are heated from the outside by tungsten wires inside the vacuum but at a distance from the crucible. These wires are connected to an external power supply, while the ovens are heated by running power through these wires. This allows thermal radiation from the wires to heat the oven in vacuum without thermal contact. For the home-built oven, the crucible and nozzle are heated separately. Although they are in thermal contact, the nozzle can be clogged if it is not significantly hotter than the crucible, where [25] can be seen for more details. The commercial oven is controlled by a separate temperature controller with PID controls which makes it significantly easier to control. Both systems use water-cooling to control temperature, the home-built has copper pipes coiled about the oven housing, while the commercial oven has its own water-jacket for cooling. Both are cooled by Van Der Heijden chillers. [1]

The Lambert-Beer law tells us how much light we expect to be absorbed for a given atomic beam. This absorption is measured by reading photo-diode (PD) voltages before and after the chamber and the setup can be seen in Fig. 3.3. The optical depth of the sample is determined from the ratio between the two, which accounts for changes in laser intensity over time, particularly as the intensity of the laser can change as the frequency is varied. The laser frequency was scanned 2-3 GHz from the resonant frequency in order to capture the full velocity ensemble and a region of non-resonant light either side for fitting purposes.

Due to heating the commercial oven without cooling the oven had to be sent for repairs. In the interest of time this meant that the commercial oven was tested after being

[1] N.B.: There have been issues with the thermocouple of the oven becoming coated with Strontium and causing a short with the oven housing. This causes the oven to read a far lower temperature and try to heat the oven very quickly. For the adapted model a shield has been placed to reduce build-up of Strontium.

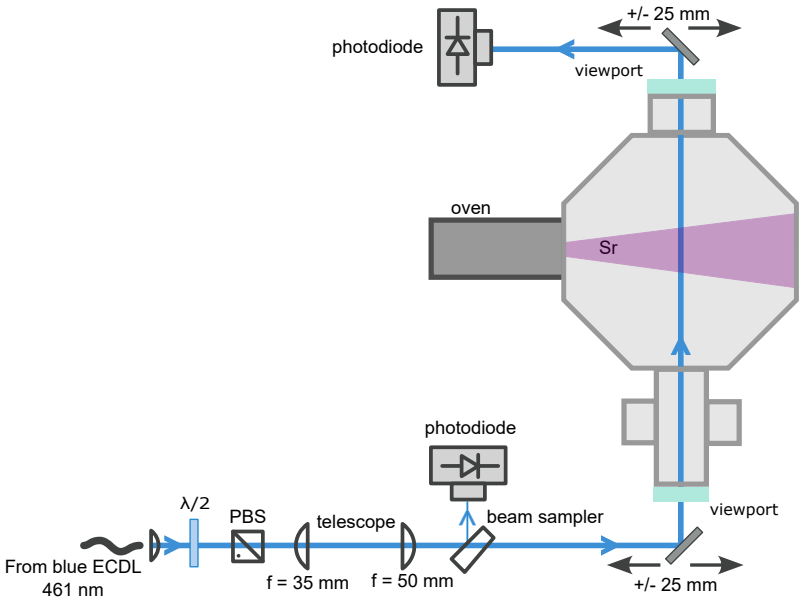

Figure 3.3 The setup used to probe the atomic beams emitted by our ovens.

attached to the 2D MOT chamber. This means that the tighter CF16 tube and internals of the 2D MOT clip the profile of the atomic beam. Thus, in order to reflect a fuller picture of atomic flux, the different measurements must be normalised for the area probed by the laser beam. Unfortunately, this removes information about the larger angular distributions for the commercial oven. These issues will be discussed in the greater detail in the following section.

These spectroscopy measurements were carried out for each oven for a variety of temperatures between $400°C - 700°C$ and also scanned in the y-axis, in order to probe how the atomic flux and angular distribution changed for different chords of the beam. With this data it is possible to give the atomic flux per unit area of the beam as a function of temperature and scan position.

3.2.2 Oven Spectroscopy Results

The spectra are plotted as a power ratio vs. laser frequency, these may be fit with the formulae above to extract the line-width and optical depth and give an analytic expression which may be integrated over, see Fig. 3.4.

The total atomic density can be extracted by integrating over the spectra:

$$n = \frac{2}{\sigma_0 D \pi \gamma} \int OD(\delta_0) d\delta_0, \tag{3.10}$$

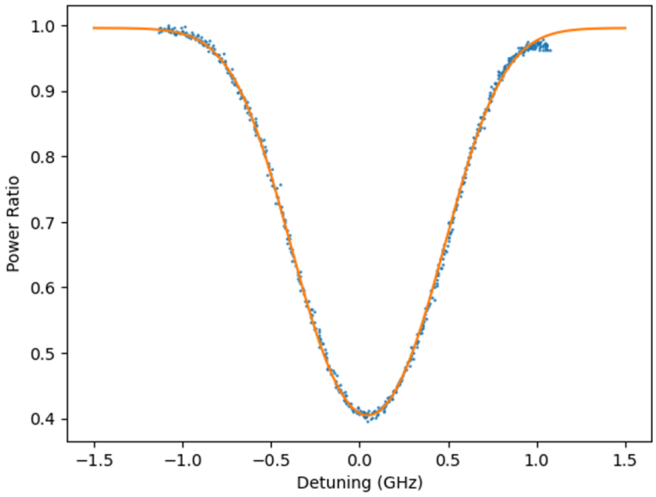

Figure 3.4 Fit of a Gaussian profile to our absorption spectra. From this we may integrate and deduce the atomic flux through the laser probe during this scan.

where D is the diameter of the atomic beam. from which our total atomic flux is

$$\phi_{Sr} = n\langle v\rangle \frac{\pi D^2}{4} \tag{3.11}$$

where $\langle v\rangle$ is the average velocity determined by our modified Maxwell-Boltzmann distribution from equation.

This allows us to plot the atomic flux rate for our ovens, see Fig. 3.5. The atomic flux closely matches those measured by Nesc Jansa [27] and appear to reflect the vapour pressure law exhibited by strontium. Both ovens have similar atomic flux per centimetre-squared. However, as the commercial oven is mounted in our 2D MOT chamber the wings of the beam are cut away. As we normalise for the area being probed, the homebuilt oven is normalised over a larger area, but this includes the wings which display a smaller atomic flux density. Thus, these normalised plots may represent a higher flux density for the commercial oven in comparison than is justified. We also see that there appears to be little difference between the pumped and un-pumped cases of the commercial.

If we examine the separate results for optical depth and line-width, see Fig. 3.6, we can see that the relationship of optical depth to temperature is similar for all oven set-ups along the centre-line of the atomic beam. The slight reduction of optical depth in the commercial oven may be due to the clipping of the MOT chamber. There are significant variations between the line-width of the spectra measured at the centre-line of each oven, with a very large change in the zero-crossing between the home-built and commercial oven. This may be due to the clipping introduced by the MOT chamber or differences in the micro-capillary arrays of the two ovens. In the clogged case we would expect to see

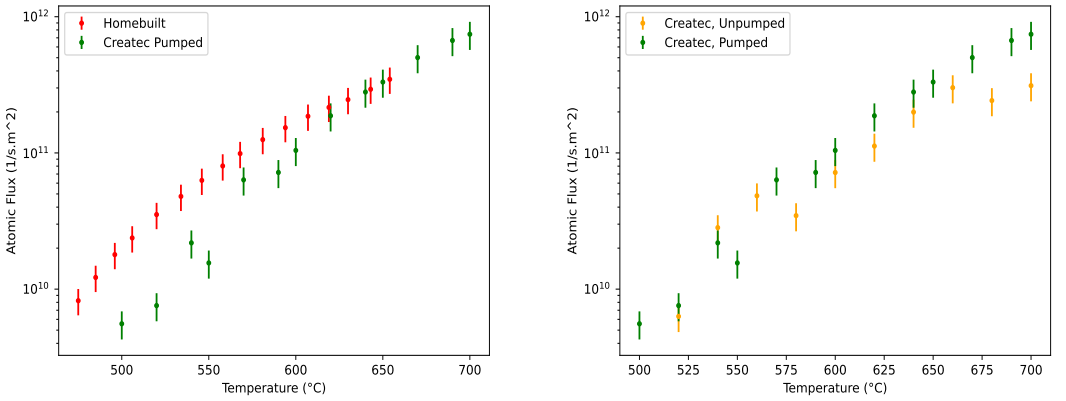

(a) Home-built and commercial oven, Pumped **(b)** Commecial oven, Pumped and Unpumped

Figure 3.5 Atomic Flux per square-centimeter of our ovens as a function of temperature

a much more diffuse atomic beam from the home-built oven. However, given that there was a significant temperature gradient of $\sim 70\,°C$ between the nozzle and crucible of the oven, and the similar atomic flux of the commercial and home-built ovens, clipping by the MOT chamber seems to the most likely cause.

The reduction in line-width-temperature dependency between the pumped and un-pumped cases is also revealing. The higher pressure in the un-pumped case means that the particles see more collisions before reaching the probe region, see Fig. 3.7.
There is no other ready explanation for such a change in a system where the only independent variable that has been change is the pressure.

After probing the centre-line of the atomic distributions, the laser probe was moved through a vertical scan of the atomic beam, see Fig. 3.8. This gives us information about the angular distribution of the atomic beam. We can see that there is a decrease in atomic flux as we move toward the edge of the atomic beam. This decrease is significantly less than that predicted by theory however, as here the entire chord of the atomic beam is being sample in each of the data points. Unfortunately, due to Strontium coating the thermocouple of the commercial oven, we could no longer perform measurements as the PID controller no longer functioned correctly. It would be interesting to examine if the line-width reduction in the pumped case is reflected in a reduction of atomic flux in the positional scans.

In conclusion, the area normalised atomic fluxes show comparable atomic flux per centimetre squared for all oven setups. While the position scans show that there is a reduction in atomic flux as we move away from the centre line, more analysis must be done to compare these values with the theory. It would be interesting to probe the wings of the atomic

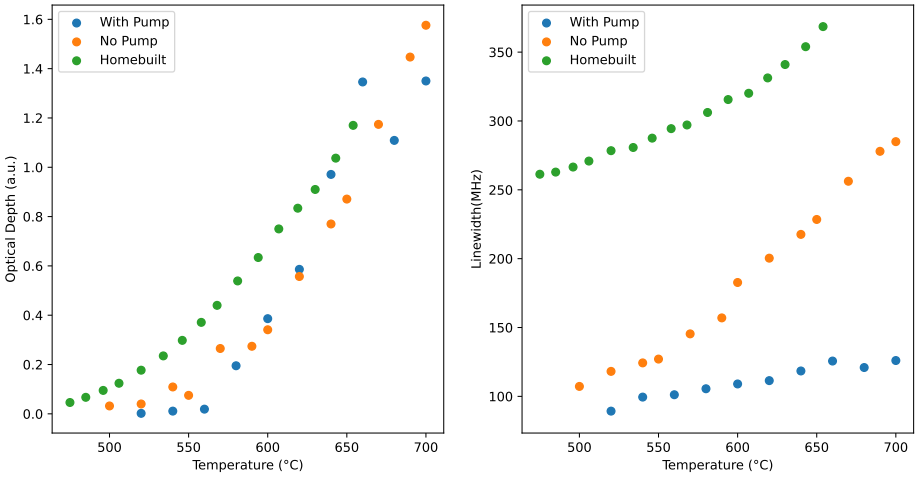

Figure 3.6 Fits for optical depth and linewidth against temperature measured at the centreline of each oven

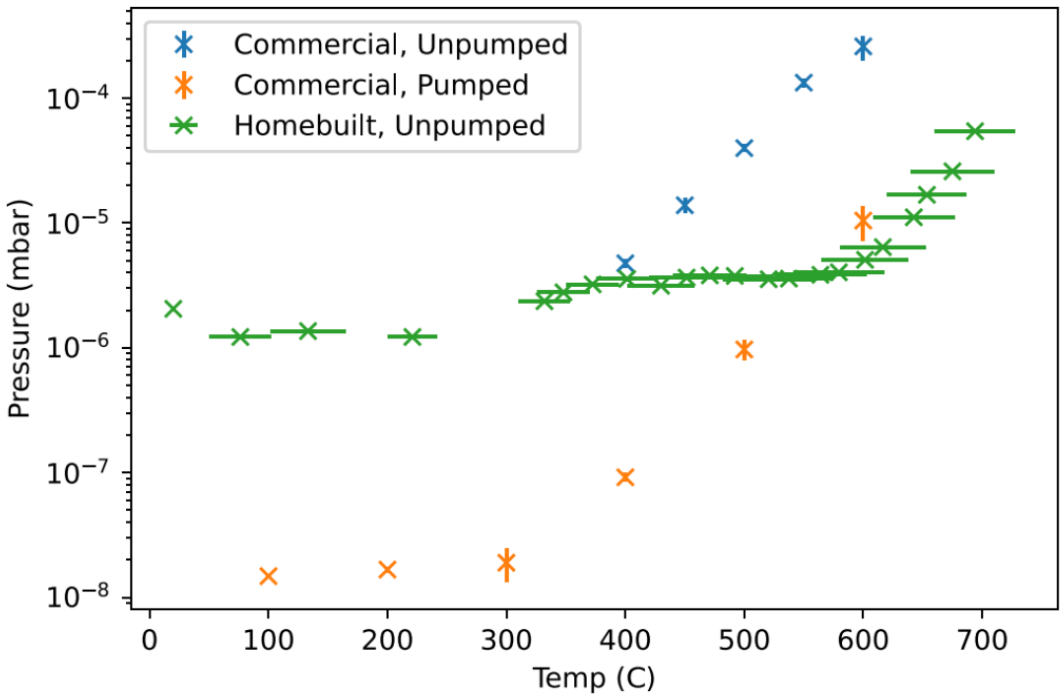

Figure 3.7 Plots of oven temperatures against pressures for the home-built oven and the commercial oven in the pumped and unpumped cases.

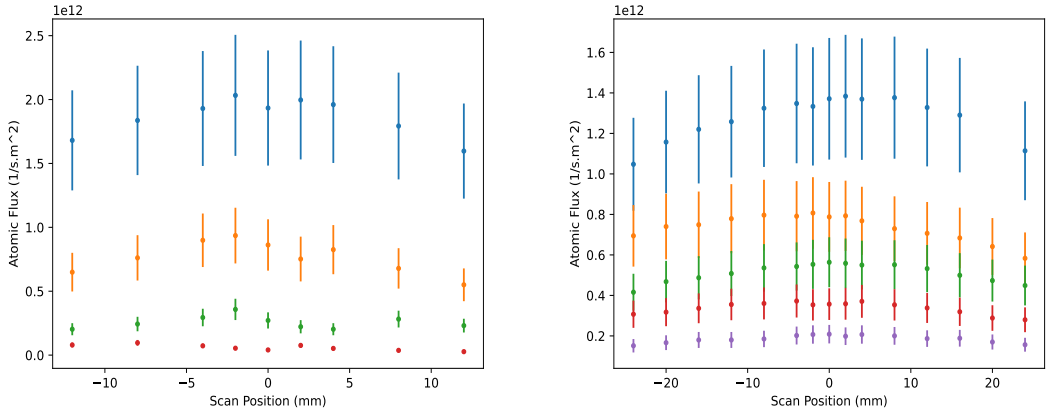

(a) Commercial oven, Un-pumped

(b) Home-built oven

Figure 3.8 Atomic Flux per square-centimeter of our ovens as a function of scan position

beam in the pumped case, as the suppression of line-width with respect to temperature suggests a tighter angular distribution. Two aspects which appear to be important are collisions of the atomic beam with residual vacuum molecules and potential clipping and reflection by the chamber walls.

Although the assumption that strontium atoms striking the walls stick due to relative low temperature of the chamber walls is an appealing one, we can observe that Strontium atoms appear to coat the chamber walls for several centimetres beyond line of sight of the oven. This implies that some scattering of atoms from the walls is occurring.

However, these concerns aside, we can see that we have a high atomic flux our trapping region and we now have demonstrated our ability to measure this distribution in space in a vacuum. This may be used to characterise ovens in future to better understand and tune MOTs for higher trapping rates.

Chapter 4

Magnetic Field Design and Measurement

Magnetic fields are central to the operation of a magneto-optical trap (MOT). Providing a spatially dependent Zeeman-shift, they alter the resonance profile of the laser light to trap atoms radially, in addition to the cooling provided by the velocity-dependent Doppler-shift. Without this radial trapping force the atoms would be cooled to the Doppler-limit but the remaining kinetic energy would cause them to diffuse through the system and greatly reduce the trapping efficiency of the MOT. Our aim is to determine the number and arrangement of the magnets for our two-dimensional (2D) MOT and simulate the magnetic fields we expect to generate from such an arrangement. With these simulations in hand we program and calibrate a three-axis magnetic sensor rig to measure the magnetic fields induced by the set-up. This test rig is used to compare the fields generated by the magnets to our theoretical predictions.

This chapter will begin with a discussion of the theory of magnetic fields as generated by both electromagnets and permanent magnets. We will then make a short comparison between the respective benefits and drawbacks of electromagnets and permanent magnets for our setup before discussing how the MagPyLib software was used to simulate proposed magnet arrangements. The programming and calibration of this rig is discussed before we measure the magnetic fields generated by the magnets while attached to the 2D MOT chamber. Having confirmed that field design was successful, the assembly and trapping of the atoms in the 2D MOT are considered.

4.1 Generation of Magnetic Fields

There are two primary means of generating magnetic fields in the lab. First is the use of electrical currents to induce a magnetic flux, second is the use of permanent magnets, whose remanence also induce magnetic flux. Here we will discuss the merits of both techniques before turning to the specifics for our MOT design.

The discovery and systematic investigation of magnetism, electricity, and their synthesis in the theory of electromagnetism, was one of the principle avenues of physical research during the 19th Century. The capacity of electrical currents to induce magnetic flux was realised in 1820, when Danish physicist Hans Christian Ørsted discovered the phenomenon [28]. This discovery was followed André-Marie Ampère's systematic investigations, which allowed him to understand this phenomenon and state Ampère's Law,

an equation to describe the magnetic flux induced by a current traveling around a loop of wire.

In the 1850s, James Maxwell took these discoveries in magnetism and, combining them with investigations of electricity, synthesised them into his eponymous laws, describing electromagnetism as a unified phenomenon. It is these laws that allow a precise understanding and control of magnetic fields for the use of experiments in the lab

$$\nabla \cdot \mathbf{E} = \frac{\rho}{\varepsilon_0}, \tag{4.1a}$$

$$\nabla \cdot \mathbf{B} = 0, \tag{4.1b}$$

$$\nabla \times \mathbf{E} = -\frac{\partial \mathbf{B}}{\partial t}, \tag{4.1c}$$

$$\nabla \times \mathbf{B} = \mu_0 \mathbf{J} + \mu_0 \varepsilon_0 \frac{\partial \mathbf{E}}{\partial t}, \tag{4.1d}$$

where $\boldsymbol{E}$ is the electric field, ρ the charge density, ϵ_0 the permittivity of free space, $\boldsymbol{B}$ the magnetic field, μ_0 the permeability of free space and $\boldsymbol{J}$ the current density [29].

For the simple case of generating the static magnetic field required for our experiment, it is sufficient to use Ampère's Law

$$\oint_\gamma \boldsymbol{B} \cdot d\boldsymbol{s} = \mu_0 I, \tag{4.2}$$

integrating about a wire loop γ with line element $d\boldsymbol{s}$ which carries a current I. To generate a two- or three-dimensional field, pairs of coils are arranged orthonormally about our region of interest. Arbitrary fields may then be generated by a linear superposition of the fields generated by the coils. While edge effects may be observed close to the coils, our measurements of the setup, to be discussed later, show that the trapping region is well modeled by our simple simulation. As such, the trapping region is in the far-field. In the next section we will discuss the MagPyLib library which may be used to give more comprehensive analysis of such edge-cases.

In the simplest case, it is possible to use the solenoid equation to predict the central, on-axis magnetic flux induced by a coil

$$B = \mu_0 \frac{NI}{l}, \tag{4.3}$$

where B is the induced magnetic flux, N is the number of windings, and l is the length of the solenoid — assuming that the area of interest is in the far-field. This allows us to quickly estimate flux values and imagine more intuitively how the magnetic flux is built up in practice, see Fig 4.1. We will have recourse to this equation later during calibration of our magnetic sensor rig.

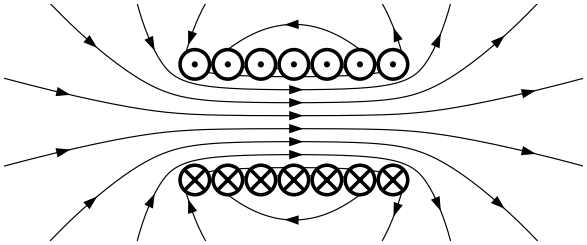

Figure 4.1 A solenoid: the circles represent current carrying wires, the arrows magnetic field lines. Adapted from [30].

Alternatively, permanent magnets can be used. Here the magnetic moment is generated by the intrinsic spins of electrons in the bulk of the magnet. In ferromagnets, such as iron, the electronic spins tend to align due to the positive sign of the exchange interaction. Conversely, in an anti-ferromagent such as Chromium, the spins favour anti-parallel arrangements due to the negative exchange interaction. While the lattice structure of such materials vary depending upon the alloy in question, the spins of such systems would tend toward a perfect ferromagnetic or anti-ferromagnetic state provided they were cooled adiabatically.

However, when a real ferromagnetic metal is quenched from a liquid to a solid, the idealised ground state will not be reached. Instead of forming a perfect crystal, individual domains appear as an expression of the excitations in the system. Without an external magnetic field — or anisotropic magnetic susceptibility in the crystal lattice — to break the symmetry of this process, the domains will still tend to form their own ferromagnetic orientation, which is determined by the mutual influence of magnetic spins local to each domain. Ferromagnets such as iron can develop an emergent magnetic orientation, while paramagnets such as aluminium require exposure to a strong magnetic field to be magnetised. Idealised sketches of the "slow" and "fast" processes can be seen in Fig 4.2. It should be noted that the emergence of grain boundaries reduce the spontaneous magnetisation of the material in question and, in turn, reduce the potential for magnetic remanence [31].

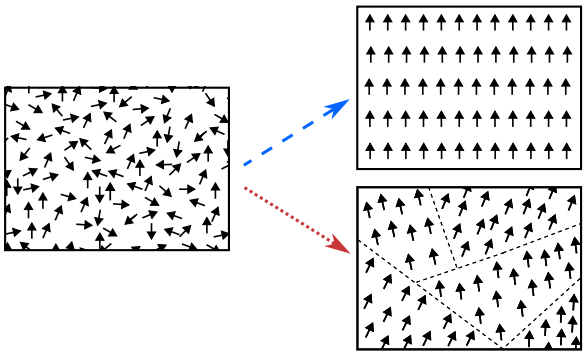

Figure 4.2 A disordered state settles into an ordered or quasi-ordered state, dependent upon adiabaticity of cooling.

Indeed, most naturally occurring ferromagnetic materials or common alloys display too little magnetic remanence to compare favourably with EM coils, in part due to the emergence of such grain boundaries. However, in 1984, teams from Sumitomo [32] and General Motors [33] simultaneously demonstrated an alloy of Neodymium, Iron and Boron (NdFeB) which produced extremely high remanence fields of up to 1.4 T, far higher than

previous alloys.

This high remanence is due to the magneto-crystalline anisotropy of the NdFeB alloy — the crystal lattice induces its own magnetic field, regardless of the direction of the applied magnetic field. Thus, a NdFeB magnet (hereafter referred to as a Neodymium magnet) has a pre-determined orientation of its magnetic field to which the spin-orbit coupling of valence electrons align spontaneously. While heating past the Curie temperature of such a material would significantly reduce it's remanence, subsequent cooling will see the spins once again align with the magneto-crystalline anisotropy. The lattice's intrinsic magnetic field shifts the hysteresis curve from the origin and significantly augments magnetic remanence.

Such macroscopic anisotropy is created by grinding the Neodymium ingot into a fine powder, on the scale of a few microns, before the powder is aligned in a magnetic field and compressed perpendicular to the direction of magnetisation. The block is then sintered, remaining under the influence of the strong magnetic field. This process artificially reduces the prevalence of grain boundaries and thus significantly increases the spontaneous magnetisation of the material. The result is a permanent magnet of very high remanence, strong enough that small stacks can generate magnetic fields comparable, and even larger than, electromagnets powered by hundreds of Ampères.

This concludes a review of two methods of generating magnetic fields in the lab. Electromagnets are an active method — requiring current flows — while permanent magnets are a passive method, requiring suitable arrangement in space of magnets with sufficient remanent magnetic fields. Both have their benefits and their weaknesses, to be discussed in the following section, as the design of magnetic fields for the MOT are considered.

4.2 Magnetic Field Design

To achieve a 2D MOT, we need to generate a strong quadrupole magnetic field gradient about our MOT in the X and Z-axes, leaving a null-field along the Y-axis. One of the first decisions in the design of a 2D MOT is which method will be used to generate the required magnetic fields.

The literature shows a number of ways to realise a 2D MOT. Since the early 90s, Ioffe coils have been used to provide the trapping for a 2D MOT, while additional anti-Helmholtz coils have been used to confine the final dimension when a 3D MOT is desired. [34] The Ioffe coil method has been used to generate trapping regions of almost 10 cm which run parallel to the effusion velocity of the atoms, and in turn generate faster atomic loading rates.[35] Another method is to use arrays of Neodymium magnets to provide the trapping fields. [36, 13]

These examples show us the relative merits of each solution. Ioffe coils generate large,

homogeneous and easily tunable magnetic fields. When the atoms are loaded parallel to the null-axis of the 2D MOT, they can trap atoms very efficiently. However, they require large amounts of electrical current, expense, and often water cooling to function, while the magnetic fields they generate are sensitive to current noise.

Neodymium magnets solve many of these issues; they are completely passive, requiring little effort to install and maintain, and do not suffer from significant sources of noise — although the fields they generate do drift with temperature. Another positive aspect is the compactness of Neodymium magnets; a set of 4 small stacks (say, 3-12 magnets) can generate magnetic field gradients on the order of 10 G/cm, comparable to 2 pairs of water-cooled coils using currents of 250 A. On the other hand, permanent magnets are not perfect. They cannot be easily tuned and generating homogeneous fields can be difficult if a simple 4 stack array is not sufficient. As our trap loads its atoms perpendicular to the trap axis, and is intended to be compact, we decided to use permanent magnets to generate our quadrupole field.

With our method decided upon, we turn to simulating our setup in order to ensure it provides the required fields.

4.3 Magnetic Simulations

We used the python library MagPyLib to simulate the magnetic fields needed to trap our atoms.[37] Here we discuss the theoretical underpinnings of theses numerical methods before discussing the details of our simulation. The results of our simulations are shown, after which we validate these simulations with physical measurements in the next section.

In the magneto-static case – where all currents are in the steady state – magnetic fields become conservative and may be expressed as a magnetic scalar potential Φ_m

$$\nabla \times \boldsymbol{H} = 0, \tag{4.4a}$$

$$\boldsymbol{H} = -\nabla \cdot \Phi_m, \tag{4.4b}$$

where $\boldsymbol{H}$ is the magnetic field strength.[29] These equations may be solved by integrating over the magnetization distribution

$$\Phi_m(\boldsymbol{r}) = \frac{1}{4\pi} \int_{V'} \frac{\nabla' \cdot \boldsymbol{M}(\boldsymbol{r'})}{|\boldsymbol{r} - \boldsymbol{r'}|} dV' + \frac{1}{4\pi} \oint_S' \frac{\boldsymbol{n'} \cdot \boldsymbol{M}(\boldsymbol{r'})}{|\boldsymbol{r} - \boldsymbol{r'}|} dS', \tag{4.5}$$

where $\boldsymbol{r}$ denotes the position, V is the magnetized volume with surface S and normal vector $\boldsymbol{n}$ to the surface. The first integral describes the potential induced by the volume current, while the second the potential induced by the surface current. Magnetic fields induced by steady currents may be derived using the Biot-Savart law

$$\boldsymbol{B}(\boldsymbol{r}) = \frac{\mu_0}{4\pi} \int_{V'} \boldsymbol{J}(\boldsymbol{r'}) \times \frac{\boldsymbol{r} - \boldsymbol{r'}}{|\boldsymbol{r} - \boldsymbol{r'}|^3} dV'. \tag{4.6}$$

To solve these equations it is common practise to use numerical methods such as finite or boundary element calculations. These can require significant time or computational power to complete, depending upon the complexity of the problem. However, it has been shown that analytical methods can provide efficient solutions for simple geometric volumes and current loops.[38, 39] In cases where the system may be represented by a superposition of such elements, this analytic approach gives excellent approximations with minimal computational load. This is the approach taken in the python library MagPyLib.

MagPyLib allows us to define and manipulate objects such as electrical currents and magnetic volumes in three-dimensional space and calculate the resultant magnetic fields using Maxwell's equations from the observer reference frame. The field induced by a stack of 5 magnets, with a remanence of 1400mT and plot in the XZ and XY planes may be shown, where each individual magnet is modelled after those we use in the lab, a 25x10x3 mm cuboid Neodymium magnet. The results of the simulation can be seen in Fig. 4.3. Note that in the XY plane the vectors are not plotted, only the magnitude of the field; as the magnetic field points out of the page, vectors in the XY plane are just numerical noise.

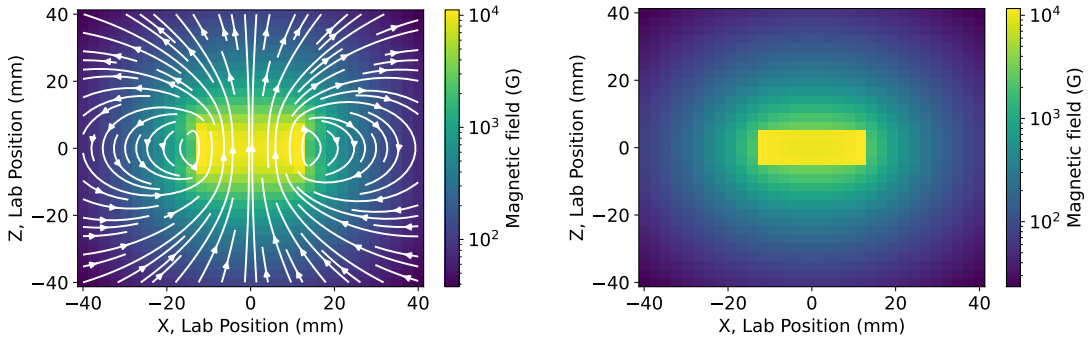

Figure 4.3 Magnetic field of a stack of 5 NeFeB magnets from different perspectives, magnetisation in the Z-direction, where panel a) shows the XZ plane and panel b) the XY plane.

The magnetic field induced by the intended array may then be constructed by the linear superposition of four stacks of 12 magnets, which is the most that can be fit in the proposed setup. The result is shown in Fig 4.4. This layout produces intended null field along the central Y-plane, appearing as a single central point when plotted in the XZ plane. The gradient in this is case is 80 G/cm, 4 times the amount suggested by earlier calculations,

which gives a large margin of error to increase or decrease the gradient as required. This demonstrates that the planned arrangement gives the desired field characteristics for trapping the 2D MOT — in panel a) of Fig 4.4 the centre of the trap shows how the quantisation axes are set along the diagonal travel of the intended cooling beams.

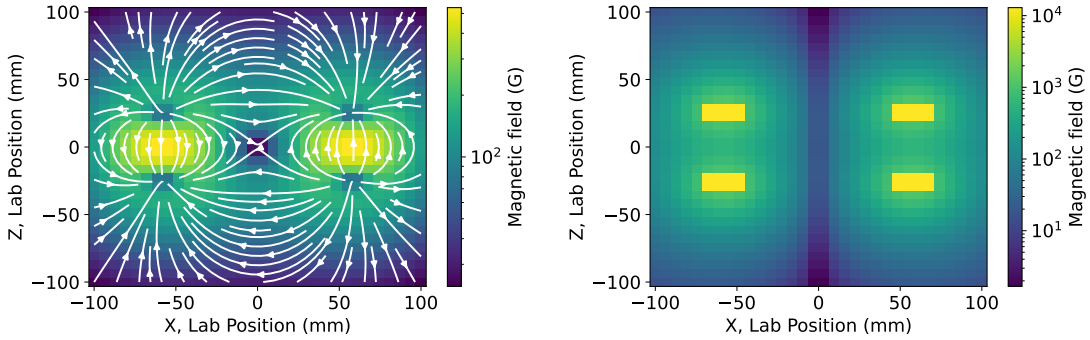

(a) **(b)**

Figure 4.4 Magnetic field induced by 4 stacks of 12 magnets, as might be arranged in the 2D MOT. Magnetisation in the Z-direction. The XZ plane is plotted in panel a) and the XY plane in panel b).

4.4 Stage and Sensor Calibration

Once the 2D MOT chamber has been assembled, everything will be under vacuum. This makes measuring the magnetic field inside the chamber challenging, and as the location of the magnetic field is central to the capture of our MOT, we need to confirm its contours to a high degree of precision. To this end, we need to confirm not only that our sensor stage accurately measures the magnetic field, but that the scans it performs are accurate to within 0.5 mm. These calibrations are discussed in the following section.

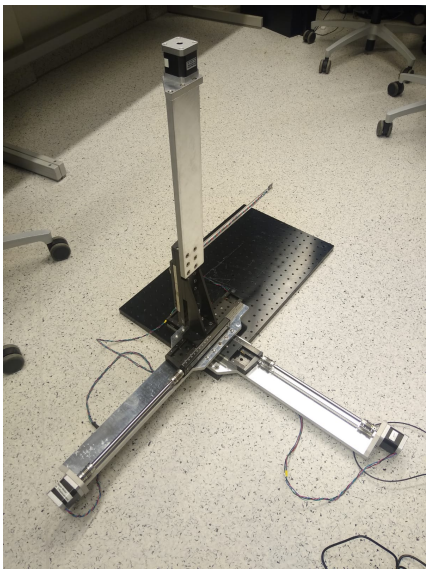

Figure 4.5 Three-axis stage.

The heart of the sensor rig is the MLX90395 IC chip. It uses a three-axis flux gate sensor to detect the magnitude and direction of magnetic fields. While we have sensitive and trusted Sensys flux gate sensor in the lab, these are too bulky to measure inside our MOT chamber and cannot measure above 10 G, whereas the MLX90395 is small

enough to fit inside our chamber and can measure fields of over 100 G. We mount the sensor on a plastic wand, to reduce influencing the magnetic fields under test. The sensor is mounted on a three-axis stage, seen in Fig. 4.5.

We read out the probe using an Adafruit Feather micro-controller via USB to the control computer. The sensor probe is mounted on 3 arms, each translatable by a lead screw turned by a stepper-motor mounted on the end of each arm, allowing the sensor probe to be moved anywhere within a 100 mm^3 range with a precision of up to 0.5 mm. Each motor is driven by a stepper motor (SparkFun Big Easy Driver)[1], each connected to the stage micro-controller (Leonardo ETH Arduino), as shown in Fig. 4.6. We control the stage with a script which simultaneously reads from the magnetic field sensor. More detail on the stepper motor and drivers can be found in Ref.[26].

Our script sets the stage to raster through a given plane while the sensor takes measurements of the magnetic field depending upon the resolution that has been set. Calibration of the stage motion is achieved using the scales on each of the axis arms. Rigorous testing showed that although large, quick movements are relatively reliable, the only way to achieve 0.5 mm precision is by using single steps at the smallest step size of 1.

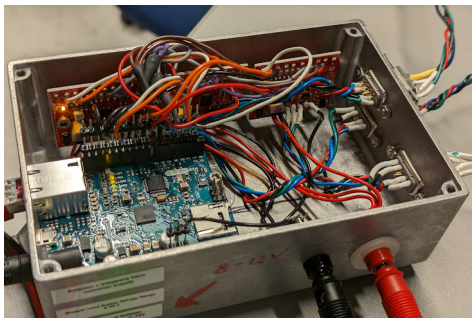

Figure 4.6 Stepper drivers and ETH Leonardo micro-controller for stage control.

Further, depending upon the desired precision required of the magnetic sensor, there can be issues with saturation effects. The readout of the MLX90395 chip has a 19 bit register but it can only read out 16 bits at a time. This limitation can cause bit-flips to occur at high magnetic field levels. To avoid this, the resolution settings on the MLX must be changed via functions on the C++ script flashed onto the sensor, in the case that such saturation effects appear. A consistent theme during this stage of work was that issues would often be found in the interstitials between one system and another, whether it was the pins of the stage drivers or the firmware which set resolution settings for the MLX sensor. Checking the "seams" between systems proved to be a reliable place to begin troubleshooting.

The last aspect of sensor calibration is to compare the readout to a second, trusted sensor. This was done by setting up a pair of solenoids and running a range of currents through them, seen in Fig. 4.7. A Sensys sensor was then used to measure the magnetic

[1]Note that for the Big Easy Stepper driver, and many similar ICs, PIN 13 is reserved for Ethernet communications. This means that a system that uses PIN 13 may be perfectly functional until it is switched to Ethernet communications... whereupon it stops functioning without explanation. This is even less fun than it sounds. Try to avoid using PIN 13 unless you need to.

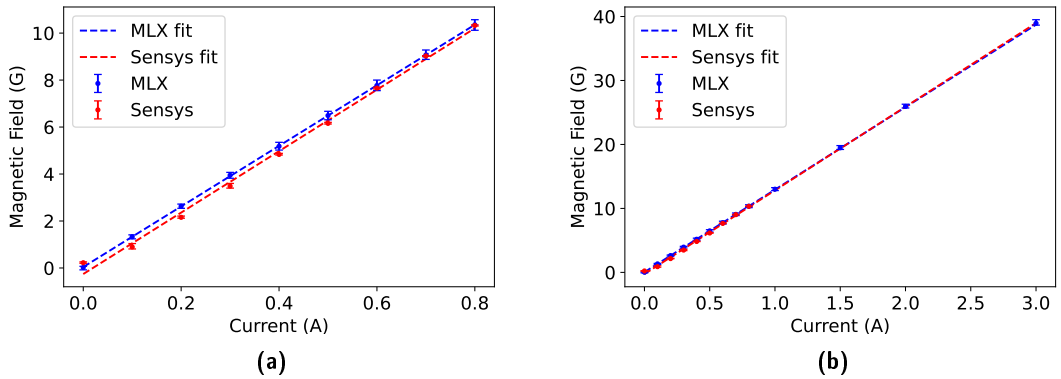

Figure 4.8 Calibration of MLX against Sensys. a) shows limited scan at extent of Sensys range while b) shows the full scan.

field generated by the solenoid along each vector. The setup displayed a plateau of magnetic field strength in the centre of the solenoid, giving assurance that edge effects were minimised.

The MLX90395 sensor was then placed in the same position and again the strength of the magnetic field for a similar range of currents were measured. Fits for the two sensors show a close match and confirm that the MLX90395 chip is well calibrated, as can be seen from Fig. 4.8. Although the Sensys probe does not share the large range of the MLX, larger currents and thus magnetic field gradients were measured using the MLX to confirm that the response remained linear.

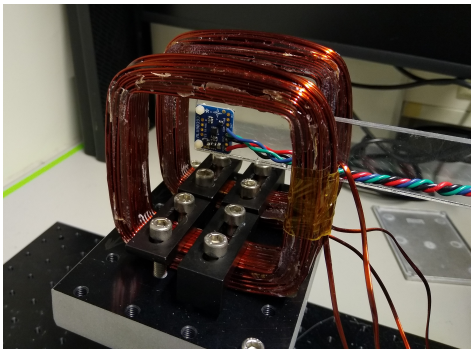

Figure 4.7 MLX sensor under calibration.

4.5 Chamber Measurements

Once the calibration of the sensor was completed our magnets were mounted onto the MOT chamber. As the metal magnet mounts were still under construction at this time, 3D printed duplicates were made. A full stack of 12 magnets were mounted in each stack and moved to the centre of their travel before being mounted into the MOT chamber. This done, the chamber was mounted upon a breadboard and the rig prepared to measure the magnetic field induced was in the XY, XZ and XY planes. The rectangular sensor wand was found to limit the translation of the sensor within the MOT chamber itself. The wand was replaced with a cylindrical rod with a notch cut into the top, into which the MLX chip was mounted.

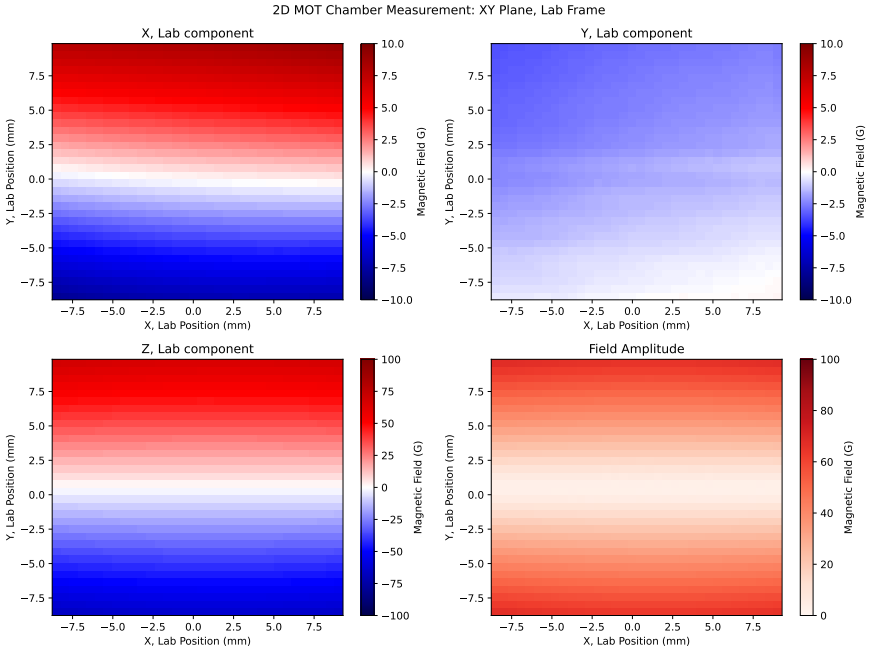

Figure 4.9 XY Scan of our magnetic arrangement

After performing coarse measurements to confirm that the null-field lay where we expected it to, the wand was moved to a corner of the MOT and set to raster through the plane to be scanned. We can see the result of these measurements on the following pages in Figs. 4.9 4.10 4.11. Here the colour scheme is changed to more clearly show the distinction between positive and negative vector fields.

The scans have been corrected for slight misalignment of the sensor wand and closely match our simulations, shown in Fig.4.12. There is a larger measured magnetic field than simulated, possibly due to magnetic fields induced in the MOT chamber itself. Although the chamber is built of low-permeability stainless steel, the magnets have a remanence of 1400 mT and in close proximity to such a large volume of steel there may be an appreciable extra magnetic field induced.

There is also a slight offset in the centre of the XY scan. This is partly due to the difficulty in centring the sensor probe at the beginning of each scan, but it should also be noted that the null point of the MOT chamber is slightly ambiguous due to uncertainty of where the MLX measured fields. Thus, although our field scans have a relative precision of 0.5 mm, there is an absolute uncertainty of up to 2 mm. This must be borne in mind during MOT trapping.

With the oven and the magnetic fields well understood, it is possible to begin construc-

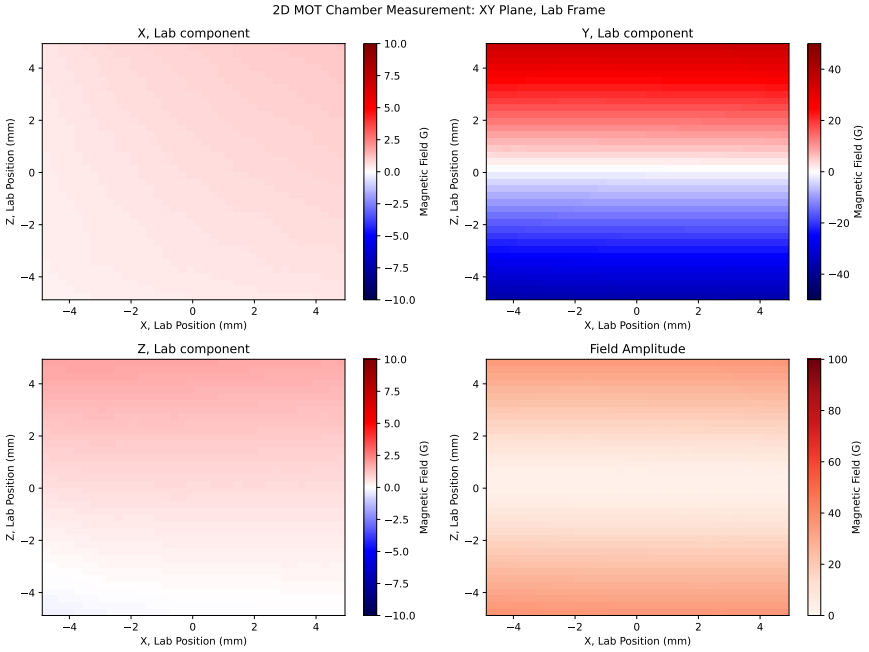

Figure 4.10 XZ Scan of our magnetic arrangement

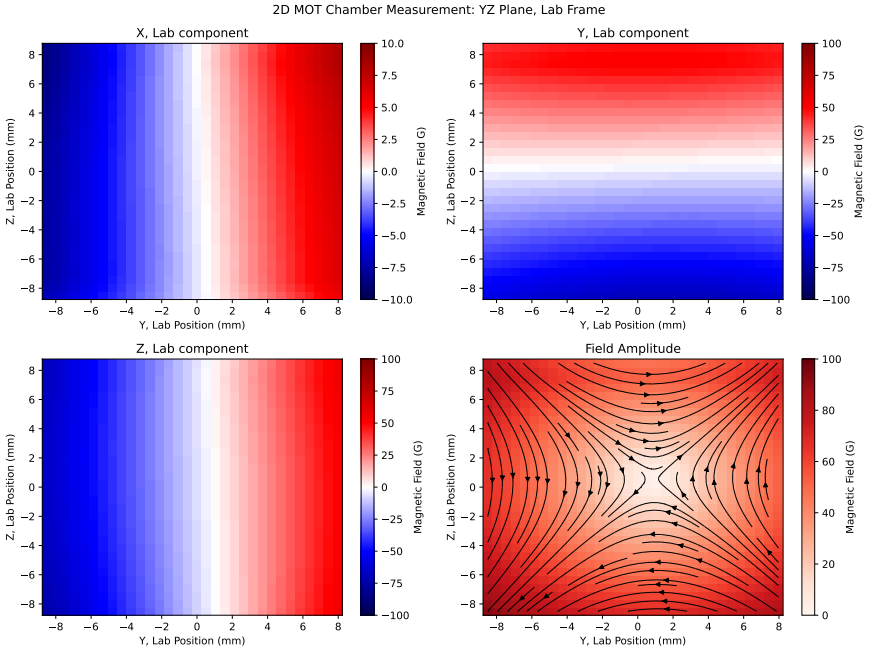

Figure 4.11 YZ Scan of our magnetic arrangement

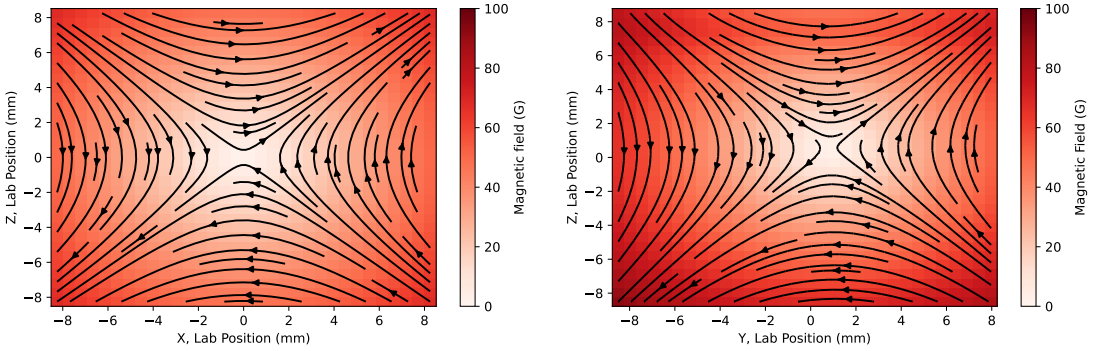

(a) **(b)**

Figure 4.12 Comparison of our simulated YZ scan (a) and our measured YZ scan, (b).

tion of the MOT chamber itself. Once the chamber is assembled and the vacuum achieved we will be able to trap the MOT. These steps will be discussed in the following chapter.

Chapter 5

MOT Assembly and Trapping

Execution

5.1 Vacuum Chamber Assembly

Our home-built vacuum chamber is centred around the stainless steel octagon of the MOT chamber to which the remaining components of our vacuum chamber are attached. The design can be seen in Fig. 5.1. On four alternating sides of the octagon, threads for CF40 flanges are sunk directly into the chamber and used to mount viewports for the cooling beams. The remaining sides have a CF16 pipe welded to them, from which a CF40 flange is attached. This arrangement allows the oven to be mounted as close to the chamber as possible, to maximise the solid angle of atomic flux we may trap in the atomic beam, and ensures that the viewports for the cooling beams can be mounted comfortably.
CF16 flanges are mounted to the two faces of the octagon — eventually these will be used to transport trapped atoms from the 2D MOT to the subsequent 3D MOT.

The last key feature of our central MOT chamber are the large cut-outs which will house our Neodymium magnets. This mounting scheme brings the magnets as close as possible to the trapping region and reduces the number of magnets required to produce our magnetic trapping field, minimising the influence of these fields on later stages of the experiment. These magnets have their own mounts which adjust the physical position of the magnets to centre the null-field and, by extension, the 2D MOT.

Before chamber assembly, all parts were carefully cleaned following the procedure in Ref. **??**. The vacuum chamber was then assembled according to the plan shown in Fig. 5.2 (a).

The oven is connected to one of the CF40 flanges with a CF16 extension. This extension allows the joint to be tightened while minimising the distance between the oven nozzle and trap centre. As the atomic beam has an angular distribution, as described in Chapter 3, the chamber is designed to mount the oven as close as possible to the central trapping region. This maximises the solid angle of atoms we can trap. A blind flange is mounted opposite the oven and four CF40 viewports are mounted at 45 °to the oven's facing to allow the cooling beams to enter the vacuum chamber. These viewports have an anti-reflection coating to minimise the reflection of the blue laser beams.

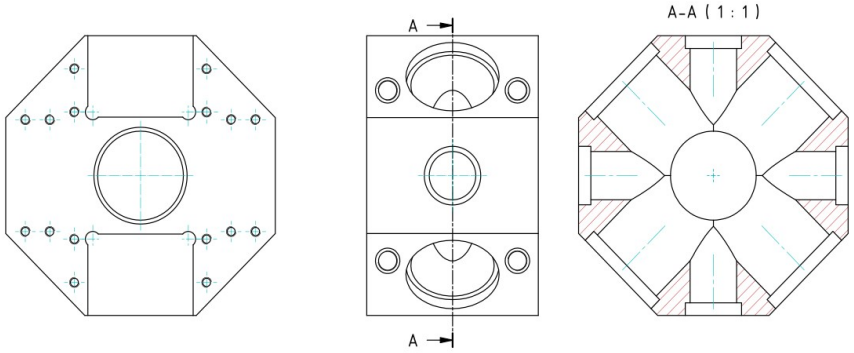

Figure 5.1 Engineering drawing of the main vacuum chamber.

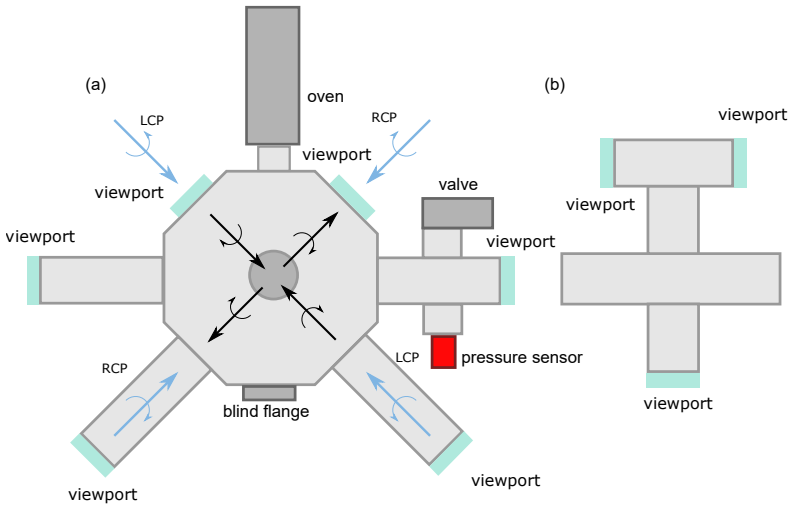

Figure 5.2 Illustration of the assembled vacuum chamber. (a) The top view. The oven is placed close to the center of the chamber. We use coated windows to enable the laser beams to enter the vacuum chamber. We can attach a pump via a valve and we detect the pressure in the chamber with a pressure sensor. (b) Side view. We mount a window below the chamber and a T-piece at the top. This will enable us to characterize the 2D MOT and the push beam.

Straight connectors are placed between the viewports opposite the oven and the MOT chamber, moving these viewports out from line-of-sight from the oven nozzle to avoid them being coated with strontium. A straight connector is attached opposite a four-way cross perpendicular to the oven and uncoated viewports are attached to the extremes of these connectors, which we use for absorption spectroscopy of the atomic beam and to observe the 2D MOT. To the four-way cross an angle valve and a pressure sensor (Pfeiffer vacuum, PKR 361) are connected, allowing us to pump down the chamber and measure the pressure in the vacuum chamber.

Figure 5.2 (b) shows an illustrates the side view of the assembled vacuum chamber. At the bottom of the chamber, we mount a CF16 viewport, intended to launch the push beam, but for now used to observe our 2D MOT. The first flange will have a viewport mounted for a kick-beam while the atoms kicked by this beam will travel down the second toward T-piece to be used for absorption spectroscopy of the resulting atomic beam.

We connect a turbo pump to the angle valve and pump out the chamber. While we are pumping, we typically reach pressures of about 1×10^{-8} mbar when using the home-built oven. So far we have not baked the chamber. However, we expect that the pressure will be significantly lower by baking. When the valve to the turbo-pump is closed, the pressure increases over the course of a few minutes from about 1×10^{-8} mbar to about 1×10^{-7} mbar.

We have carried out leak tests and eliminated all the leaks that we were able to eliminate. However, we noticed that the commercial oven has a small but consistent leak between the cooling jacket and the base plate of the oven. Although this joint has been replaced several time the leak has persisted. With the commercial oven have only reached pressures of about 1×10^{-7} mbar while pumping the chamber.

It should also be noted that strontium displays a "getter" effect, reducing the pressure in the chamber by a factor of 2-3 when an oven is run hot enough to vapourise the atoms. The pressure then steadily creeps up due to out-gassing until the oven is heated again and the getter effect repeated.

Oven Replacement

While characterising the oven with absorption spectroscopy, the commercial oven's thermocouple failed. The thermocouple gave false readings that were too low when compared to the pressure of the chamber. As a result, the controller provides too little power to heat required temperatures and has no reliable way of measuring the real temperature inside the oven.

To resolve this issue, the commercial oven was removed and the home-built oven installed in its place. After this procedure was carried out, the system was found to down

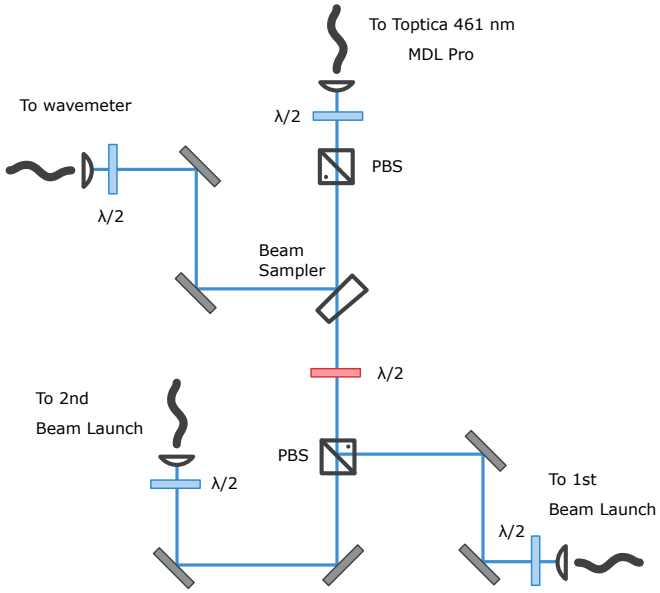

Figure 5.3 Laser Distribution Board, the red $\lambda/2$ waveplate is used to adjust power between the arms to calibrate for imbalances in fibre coupling efficiencies.

well — no leakages were found after a thorough leak-check. However, a large 8-was cross which is integrated into the home-built oven for testing purposes increases the distance from oven nozzle to trapping region to around 40 cm. In contrast, the commercial oven has a nozzle-to-trap distance of 10 cm. The result is that, with the home-built oven mounted, our trapping region captures a much smaller solid angle of our atomic beam and we expect a significant reduction in trapped atoms as would be anticipated with the commercial oven. Once the 2D MOT is functional, it will be simple to replace the repaired commercial oven — we have a good deal of experience on this front.

5.2 MOT Assembly and Trapping

Light for the cooling beams are provided by a Toptica 461 nm laser with a current of around 425 mA for an output power of about 210 mW after the fibre. The light is sent to a distribution board where a beam-sampler is used to pick-off light for the wave-meter before the power is split, using a PBS, between the two arms of the MOT. The input powers are calibrated to balance the power due to uneven coupling efficiencies. Laser power coupled into the first and second beam launchers are about 100 mW and 80 mW respectively, which after coupling to the fibres gives an output power of 45 mW in each arm.

Trapping our MOT requires beam-launches that will focus our cooling lasers into the MOT chamber with the correct beam waist, intensity and saturation parameters. Our

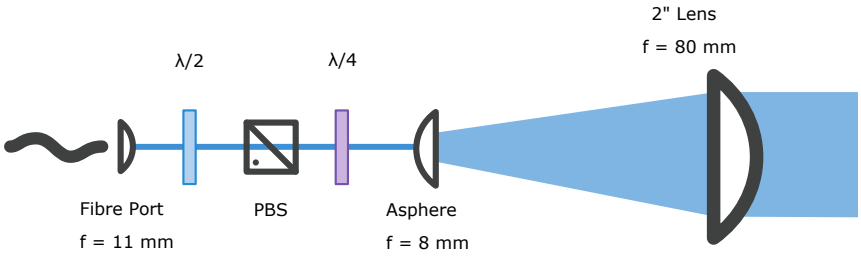

Figure 5.4 Final design of our beam launch. After a fibre-port with an f = 11 mm collimation lens we place a $\lambda/2$ waveplate and a PBS to clean the polarisation of the light. This is then sent through a $\lambda/4$ waveplate, allowing the circular polarisation of the light to be adjusted, as needed for directional selectivity for radial trapping of the MOT. The beam is then broadened with a telescope consisting of an 1" diameter aspheric f = 8 mm lens and a 2" diameter f = 80 mm lens. By adjusting the position of the final lens, the beam can be focussed or de-focussed as required to maintain balanced radiation pressure on the MOT.

beam launches must provide Gaussian light profiles of radius between 15 mm and 25 mm, with circular polarisation of the light and adjust the focussing of the cooling beams to counteract for intensity loss through the trap. This circularly polarised light will be used to provide the trapping for our 2D MOT.

After out-coupling from a fibre-port (ThorLabs PAF2PA-11A,) the light is passed through a half-waveplate, a polarising beam-splitter (PBS) and a quarter-waveplate. The half-waveplate allows us to maximise transmission of linear polarized light through the PBS and reflect any unwanted light, cleaning the polarisation. With the quarter-waveplate light is circularly polarized. We can control the angle and collimation length of the collimation lens inside the fibre-port with three screws. After the fibre-port and the waveplates, we add a telescope consisting of an aspheric lens with a focal length of f = 8 mm and a 2" diameter f = 80 mm lens, as can be seen in Fig. 5.4. This compact realisation gave us a beam width which showed relatively good profile characteristics when imaged with a Cinogy CinCam CMOS Nano Beam Profiler, as seen in Fig. 5.5. By changing the position of the final lens we can vary the beam diameter between 15 mm and 25 mm.

As the beam travels through the various components of our MOT set-up, we expect to see a reduction in intensity throughout the beam's passage, particularly due to resonant atoms in the chamber. In order to counteract this effect, a slight focussing can be applied to the cooling beams if necessary. A steady decrease in beam diameter will counteract loss of intensity and ensure that atoms in the 2D MOT region see a balanced laser pressure from both sides.

Retro-reflectors and $\lambda/4$ waveplates are added to the windows opposing the cooling beams. These provide the circular polarisations needed to trap the atoms. The distance

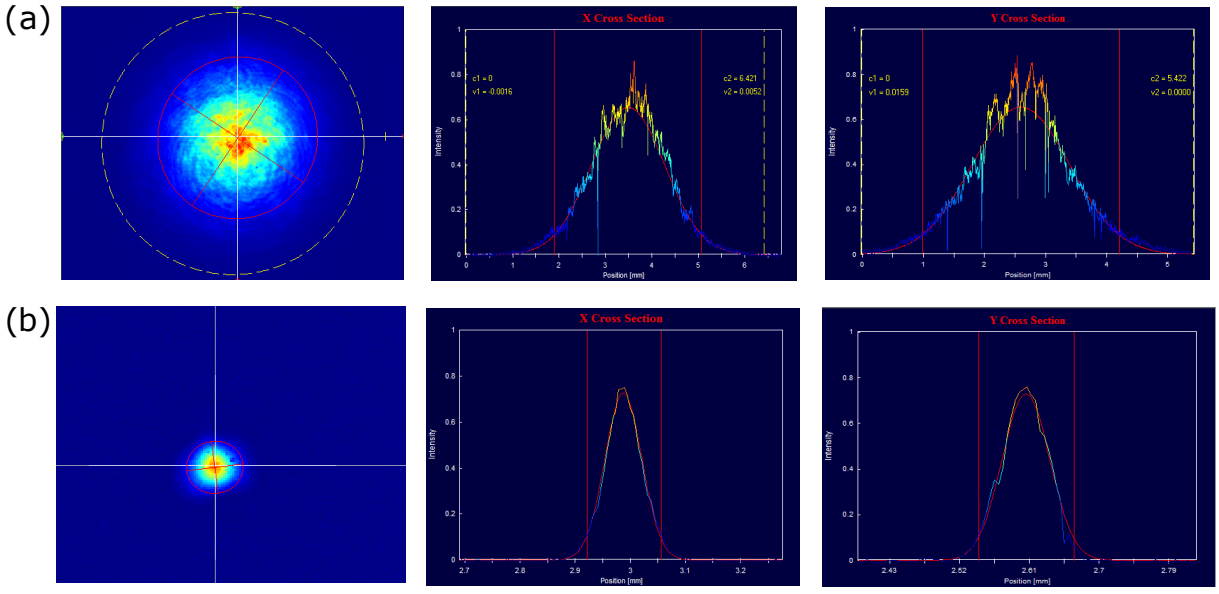

Figure 5.5 Beam profiles as measured by a beam profiler. Panel a) shows the profile after our last magnification lens, focussed upon the beam profiler at a distance of 440 mm. The X- and Y-cross sections include a Gaussian fit. Although noisy, the fit is acceptable for our purposes. We would expect to see some inhomogeneity in the MOT as a result of these beam defects. Panel b) shows the beam profile without the telescope, after our waveplates and PBS. Here the image is taken at a distance of 360 mm and matches the Gaussian profile very well.

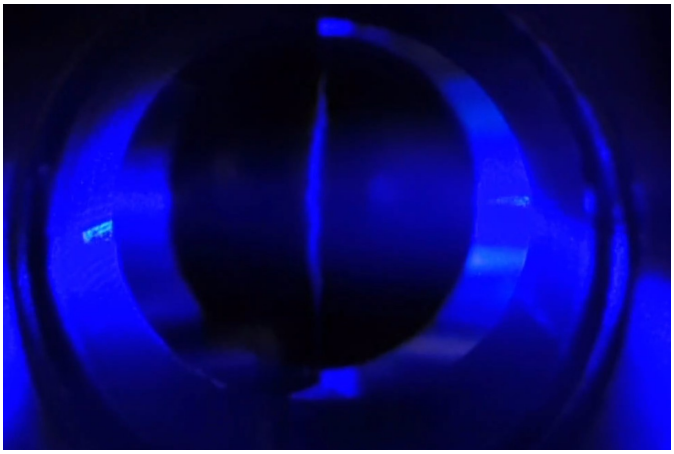

Figure 5.6 Trapped MOT

between the aspheric and final lenses are set to 90 mm to slightly focus the beam and counteract intensity loss due to reflection or absorption.

The beams are centred on the retro-reflector using the small amount of light transmitted through the reflectors as a guide. The magnet housings had three magnets placed in each corresponding to a magnetic field gradient at the trap centre of around 20 G/cm, according to our simulations. The MOT was trapped with the crucible at 493 °C and nozzle at 553 °C, at a pressure of 5.6×10^{-7} mbar and a frequency scanning range of 650.50370 - 650.50385 THz. With this set-up we see the MOT coalesce and vanish as the laser moves in and out of trapping resonance. ThorLabs Zelux cameras were setup to view the MOT from below and through the absorption spectroscopy arms. With the aid of these cameras, the MOT can be centred by adjusting the position of the magnets within their adjustable housings.

We can see our first trapping of the MOT, in colour, in 5.6

5.3 Characterisation

Images were taken of the MOT from the side and below, as can be seen in 5.7 We characterise the MOT by imaging and fitting a 2D Gaussian to each image taken from below the MOT. Plotting the peak intensity of these fits, maximum fluorescence occurs at 650.50375 THz which corresponds to a detuning from the resonant frequency of 70 Mhz or 2.3γ. This maximum occurs at the same frequency with our cooling beams at half the power, suggesting insensitivity of our trapping frequency to beam power. As the frequency is scanned we see an initial peak as the MOT coalesces before vanishing. This is the point at which our lasers are on resonance and no longer give a trapping force. As the scan is continued the MOT reforms showing that the MOT is, with respect to fluorescence,

symmetric to detuning. This is suprising, as it suggests that blue-detuned light is also sufficient to trap the MOT. However, if we examine 2.1 we can see that blue-detuning would flip direction from which the atoms are addressed and counteract the blue detuning.

The MOT peak intensity is linearly correlated with power, as seen in 5.9. Each data point on this fit was determined by fitting a 2D Gaussian to the intensity and taking the peak of the fit, as seen in 5.8 However, as the trapping force scales linearly with the scattering rate, it is not possible to say whether this is due to increased trapping of atoms or more light being scattered by the MOT due to increased intensity. Absorption spectroscopy would be the best method for disentangling this issue.

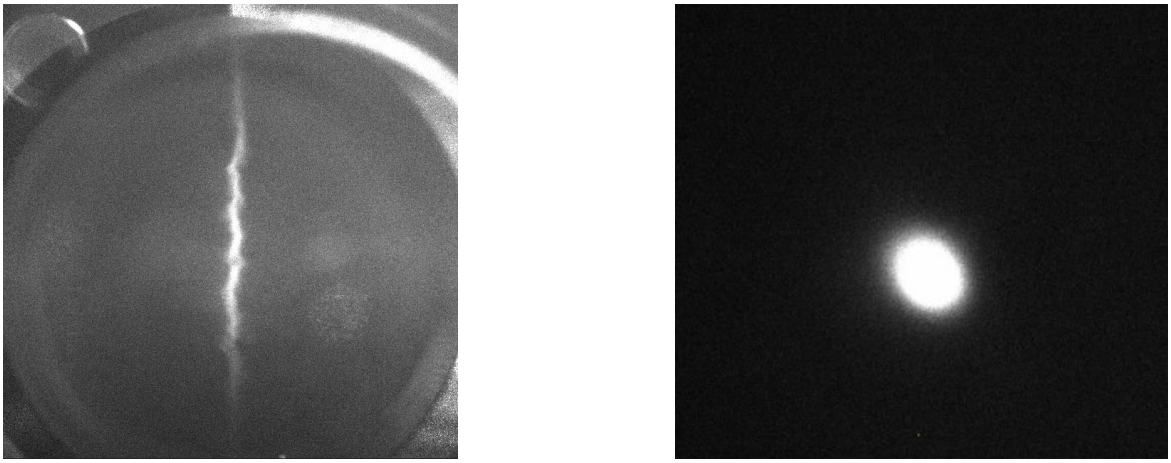

(a) (b)

Figure 5.7 Images of our centred MOT from the side a) and from below b)

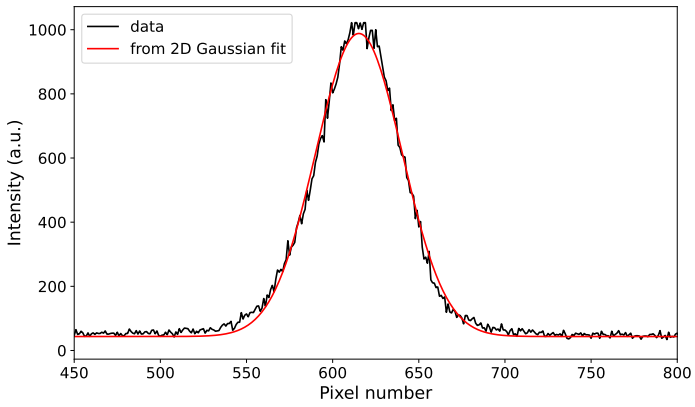

Figure 5.8 Fit of the power at 42.6 mW with a laser frequency of 650.50375 THz

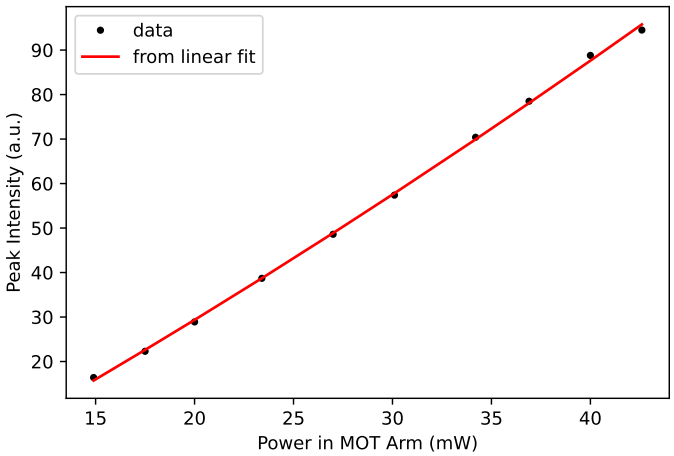

Figure 5.9 Fitted plot of our 2D MOT fluorescence as a function of laser power (in one arm.)

Chapter 6

Conclusion

We have designed and constructed a two-dimensional magneto-optical trap and demonstrated the successful trapping of Strontium atoms. After determining experimental parameters with a review of past experiments and running simulations, the MOT chamber was designed and manufactured. Two atomic sources were probed using absorption spectroscopy and confirmed to be suitable for the loading of our MOT. A magnetic test setup was established to probe the magnetic field in situ. The MOT chamber was assembled and pumped down to allow for an initial test run. With the hardware in place, the MOT was realised and its fundamental properties characterised.

Outlook

With the 2D MOT established, immediate goals are to install a push-beam and perform absorption spectroscopy on the resultant atomic beam. This will allow quantitative analysis of the beam and provides a means to optimise the flux. There are also opportunities to perform time of flight measurements to determine the temperature of the MOT. These measurements would give information about the expected loading rate.

Also, replacing the home-built oven with the refurbished commercial oven is anticipated to substantially increase the atomic flux through the trapping region and thus the atomic flux produced by our 2D MOT. The MOT loading may be improved by optical pumping of the $5s4d^1D_2$ to the fast decaying $5s8p^1P_1$ line. This high-lying state rapidly decays back to the ground state and has been shown to improve loading of a (3D) MOT by 60% [40].

We are now in a strong position to continue the development of our planned optical lattice clock.

References

[1] Bothwell, T., C. J. Kennedy, A. Aeppli, D. Kedar, J. M. Robinson, E. Oelker, A. Staron, and J. Ye. *Resolving the gravitational redshift across a millimetre-scale atomic sample*, Nature **602**., 420–424 (2022). DOI: 10.1038/s41586-021-04349-7.

[2] McGrew, W., X. Zhang, R. Fasano, S. Schäffer, K. Beloy, D. Nicolodi, R. Brown, N. Hinkley, G. Milani, M. Schioppo, *et al. Atomic clock performance enabling geodesy below the centimetre level*, Nature **564**., 87–90 (2018). DOI: 10.1038/s41586-018-0738-2.

[3] Isham, C. J. *Canonical Quantum Gravity and the Problem of Time*, Integrable Systems, Quantum Groups, and Quantum Field Theories. **602** (1993). DOI: 10.1007/978-94-011-1980-1_6.

[4] Ludlow, A. D., M. M. Boyd, T. Zelevinsky, S. M. Foreman, S. Blatt, M. Notcutt, T. Ido, and J. Ye. *Systematic Study of the ^{87}Sr Clock Transition in an Optical Lattice*, Phys. Rev. Lett. **96**, 033003 (2006). DOI: 10.1103/PhysRevLett.96.033003.

[5] Essen, L. and J. V. L. Parry. *An Atomic Standard of Frequency and Time Interval: A Cæsium Resonator*. en, Nature **176**., 280–282 (Aug. 1955). ISSN: 1476-4687. DOI: 10.1038/176280a0.

[6] Hänsch, T. W. *Passion for Precision (Nobel Lecture)*. en, ChemPhysChem **7**., 1170–1187 (2006). ISSN: 1439-7641. DOI: 10.1002/cphc.200600195.

[7] Kolachevsky, N. *et al. 2S-4S spectroscopy in hydrogen atom: The new value for the Rydberg constant and the proton charge radius*, AIP Conference Proceedings **1936**., 020015 (Feb. 2018). ISSN: 0094-243X. DOI: 10.1063/1.5025453.

[8] Loeb, A. and D. Maoz. *Using Atomic Clocks to Detect Gravitational Waves*. Jan. 2015. DOI: 10.48550/arXiv.1501.00996.

[9] Wynands, R. and S. Weyers. *Atomic fountain clocks*. en, Metrologia **42**., S64–S79 (June 2005). ISSN: 0026-1394, 1681-7575. DOI: 10.1088/0026-1394/42/3/S08.

[10] Hall, J. L. *Nobel Lecture: Defining and measuring optical frequencies*, Rev. Mod. Phys. **78**. Publisher: American Physical Society, 1279–1295 (Nov. 2006). DOI: 10.1103/RevModPhys.78.1279.

[11] Tanaka, Y. and H. Katori. *Exploring potential applications of optical lattice clocks in a plate subduction zone*. en, J Geod **95**., 93 (July 2021). ISSN: 1432-1394. DOI: 10.1007/s00190-021-01548-y.

[12] Ludlow, A. D., M. M. Boyd, J. Ye, E. Peik, and P. O. Schmidt. *Optical atomic clocks*, Rev. Mod. Phys. **87**. Publisher: American Physical Society, 637–701 (June 2015). DOI: 10.1103/RevModPhys.87.637. URL: https://link.aps.org/doi/10.1103/RevModPhys.87.637 (visited on 12/01/2023).

[13] Barbiero, M., M. G. Tarallo, D. Calonico, F. Levi, G. Lamporesi, and G. Ferrari. *Sideband-Enhanced Cold Atomic Source for Optical Clocks*. en, Phys. Rev. Applied **13**., 014013 (Jan. 2020). ISSN: 2331-7019. DOI: 10.1103/PhysRevApplied.13.014013.

[14] Metcalf, H. J. and P. Van der Straten. *Laser cooling and trapping*. Springer, 1999. DOI: 10.1007/978-1-4612-1470-0.

[15] Grynberg, G., A. Aspect, C. Fabre, and C. Cohen-Tannoudji. *Introduction to Quantum Optics: From the Semi-classical Approach to Quantized Light*. Cambridge University Press, 2010. DOI: 10.1017/CBO9780511778261.

[16] Phillips, W. D. *Nobel Lecture: Laser cooling and trapping of neutral atoms*, Rev. Mod. Phys. **70**, 721–741 (1998). DOI: 10.1103/RevModPhys.70.721.

[17] Xu, X., T. H. Loftus, J. L. Hall, A. Gallagher, and J. Ye. *Cooling and trapping of atomic strontium*, JOSA B **20**., 968–976 (2003). DOI: 10.1364/JOSAB.20.000968.

[18] Chu, S. *Nobel Lecture: The manipulation of neutral particles*, Rev. Mod. Phys. **70**, 685–706 (1998). DOI: 10.1103/RevModPhys.70.685.

[19] Wallner, F. *New Tools for Controlling Strontium Atoms with High Spectral and Spatial Resolution*, (2020).

[20] Ramsey, N. F. *Molecular Beams*. Oxford Classic Texts in the Physical Sciences. Oxford, New York: Oxford University Press, Apr. 1990. ISBN: 978-0-19-852021-4.

[21] Clausing, P. *Over den verblijftijd van moleculen en de strooming van zeer verdunde gassen*, (1928).

[22] Olander, D. R. and V. Kruger. *Molecular Beam Sources Fabricated from Multichannel Arrays. III. The Exit Density Problem*, Journal of Applied Physics **41**., 2769–2776 (Nov. 2003). ISSN: 0021-8979. DOI: 10.1063/1.1659313. URL: https://doi.org/10.1063/1.1659313 (visited on 11/17/2023).

[23] Vanier, J. and C. Audoin. *The quantum physics of atomic frequency standards*. en. Bristol: Hilger, 1989. ISBN: 978-0-85274-434-5.

[24] Inguscio, M. and L. Fallani. *Atomic Physics: Precise Measurements & Ultracold Matter*. Oxford University Press, 2015. ISBN: 978-0-19-852584-4.

[25] Staub, E. *Developing a High-Flux Atomic Beam Source for Experiments with Ultracold Strontium Quantum Gases*. en, ().

[26] Casotti, E. *A Two-dimensional Magneto-optical Trap for Strontium*, ().

[27] Janša, N. *A frequency-stable diode laser system for spectroscopy and trapping of Sr atoms*, (2016).

[28] Ørsted, H. C. *Annals of philosophy*. en. 1820. URL: https://hdl.handle.net/2027/osu.32435051156651?urlappend=%3Bseq=297 (visited on 11/27/2023).

[29] Jackson, J. D. *Classical electrodynamics*. und. 12. print. OCLC: 705218816. New York: Wiley, 1962.

[30] *Solenoid*. Publication Title: Wikipedia. URL: https://en.wikipedia.org/wiki/Solenoid.

[31] Woodcock, T. G., Y. Zhang, G. Hrkac, G. Ciuta, N. M. Dempsey, T. Schrefl, O. Gutfleisch, and D. Givord. *Understanding the microstructure and coercivity of high performance NdFeB-based magnets*, Scripta Materialia. Viewpoint Set No. 51: Magnetic Materials for Energy **67**., 536–541 (Sept. 2012). ISSN: 1359-6462. DOI: 10.1016/j.scriptamat.2012.05.038. URL: https://www.sciencedirect.com/science/article/pii/S1359646212003648 (visited on 11/28/2023).

[32] Sagawa, M., S. Fujimura, N. Togawa, H. Yamamoto, and Y. Matsuura. *New material for permanent magnets on a base of Nd and Fe (invited)*, Journal of Applied Physics **55**., 2083–2087 (Mar. 1984). ISSN: 0021-8979. DOI: 10.1063/1.333572. URL: https://doi.org/10.1063/1.333572 (visited on 11/28/2023).

[33] Croat, J. J., J. F. Herbst, R. W. Lee, and F. E. Pinkerton. *Pr-Fe and Nd-Fe-based materials: A new class of high-performance permanent magnets (invited)*, Journal of Applied Physics **55**., 2078–2082 (Mar. 1984). ISSN: 0021-8979. DOI: 10.1063/1.333571. URL: https://doi.org/10.1063/1.333571 (visited on 11/28/2023).

[34] Dieckmann, K., R. J. C. Spreeuw, M. Weidemüller, and J. T. M. Walraven. *Two-dimensional magneto-optical trap as a source of slow atoms*. en, Phys. Rev. A **58**., 3891–3895 (Nov. 1998). ISSN: 1050-2947, 1094-1622. DOI: 10.1103/PhysRevA.58.3891. URL: https://link.aps.org/doi/10.1103/PhysRevA.58.3891 (visited on 11/17/2023).

[35] Schoser, J., A. Bataer, R. Loew, V. Schweikhard, A. Grabowski, Y. Ovchinnikov, and T. Pfau. *An Intense Source of Cold Rb Atoms from a Pure 2D-MOT*, arXiv: Atomic Physics (Jan. 2002). URL: https://www.semanticscholar.org/paper/An-Intense-Source-of-Cold-Rb-Atoms-from-a-Pure-Schoser-Bataer/c4cbf2fc27f7ca62c5d0d75b951e2d07d8d797bf (visited on 11/28/2023).

[36] Tiecke, T. G., S. D. Gensemer, A. Ludewig, and J. T. M. Walraven. *High-flux two-dimensional magneto-optical-trap source for cold lithium atoms*. en, Phys. Rev. A **80**., 013409 (July 2009). ISSN: 1050-2947, 1094-1622. DOI: 10.1103/PhysRevA.80.013409. URL: https://link.aps.org/doi/10.1103/PhysRevA.80.013409 (visited on 11/17/2023).

[37] Ortner, M. and L. G. Coliado Bandeira. *Magpylib: A free Python package for magnetic field computation*. English, SoftwareX **11** (Jan. 2020). ISSN: 2352-7110. DOI: 10.1016/j.softx.2020.100466. URL: https://www.softxjournal.com/article/S2352-7110(20)30017-0/fulltext (visited on 11/28/2023).

[38] Yang, Y. *A Narrow-linewidth Laser System for the 1S0-3P2 Intercombination Transition in Strontium*, ().

[39] Camacho, J. M. and V. Sosa. *Alternative method to calculate the magnetic field of permanent magnets with azimuthal symmetry*, Revista mexicana de física E **59**, 8–17 (June 2013).

[40] al., J. S. et. *Exploring potential applications of optical lattice clocks in a plate subduction zone*, (2023).

Acknowledgements

My work in the Bloch group for this thesis has been one of the most challenging, humbling and invigorating experiences of my life. Although the going has not always been smooth, and there have been some tough times, I was always motivated to push on because of the people and culture of the group. I could never have achieved what I did without the tireless and committed support of the strontium lab and the wider group as a whole.

Sebastian Blatt has to be thanked first and foremost. You threw me in at the deep end, with what I hope was more faith than curiosity, and gave me the guidance I needed to push through the many challenges in the lab. You were never shy to turn up the heat when we needed grilling, but always made sure we didn't get burnt. If I always found myself on a team with someone half as driven, knowledgeable and focussed on the development of those around them as you, I would count myself profoundly lucky. Thank you Sebastian.

Next, thanks are due Immanuel Bloch for giving me the opportunity to work in the group. On top of providing the means and direction of the group, your work building the culture to attract and cultivate the talent and team spirit of the group is no easy task and the results show. The whole group constantly strives for excellence while remaining always friendly, helpful and selfless and I thank you being the driving will and vision behind such a group of talented and comitted scientists.

I also have to say thanks to everyone in the strontium lab. Without you, it would all have been for nought. In no particular order, because every one of you brightened my experience and taught me more than I could have hoped. Sebastian Pucher, for always having faith that I would "figure it out," your efforts to keep me focussed on the bigger picture and not sweat the small stuff, even when it took some time to get through my thick skull. Valentin Klüsener for always being ready and able to help out when things just didn't make sense, when things got tough you were always there with a laugh to lighten the mood. Andreas Schindewolf, thank you for having the patience and will to hammer me into a better scientist. I know it wasn't easy and there's still work to be done, but I'm looking forward to pushing on in the coming weeks! Thanks to Andreas Meyer and Ömer Ersahan for soldiering through with me and your constant advice and comradeship, inside and outside of MPQ, which made everything run a bit easier when times were tough. A special thanks is due to Ka Hui Goh, without whom the MOT would not have been trapped and this would be a much less interesting thesis. I hope I can repay your efforts with work on the next stage of the project and learn to emulate something of your calm focus. Thanks to Vinay Shankar, without whom the work on the oven would be

far less developed and who was invaluable in pushing the project forward. Also thanks to Saumya Shah and Klavdia Kontou, who always made my days that much brighter and gave me the opportunity to pass on some of the knowledge I learned while I was here. And, last but not least, Felix and Simone for all the company working long nights and weekends at the lab. It was always good to have a friend or two around when things were quiet, and your advice and help has been far more useful than you know.

Thanks also to Jan Trautmann, Dmitri Yankeleev, Lukas Reichsöllner and Stepan Snigirev. It will always be a regret that there was not more time to learn what you had to teach and I hope it will not be the last opportunity.

I would also like to give particular thanks to Milan, who designed the MOT chamber that all our efforts rested on and was always glad to help, even when he was extremely busy. Also thank you Anton, for always knowing what needed doing in an instant, and often getting it done just as fast. You are both responsible in no small way for the successes of this thesis. Thanks to Karsten for taking me under his wing when I was a young HiWi who didn't know up from down, it's always good to see you. Thanks also to Kristina for always helping out when there were administrative issues, of which there were a few. Your tireless efforts keep the Bloch group running smoothly and I'm sure everyone in the group feels the same, thank you.

I'd also like to say thanks to the wider group, of whom I wish I had spent more time getting to know. I've said it before and I'll say it again that the group is always a super fun and relaxing place to work because of the people who make it up. Also thanks to the group leaders, who I didn't have a lot of conact with, but who's positive influence in drive and motivation can be felt in the group, and which reflects Immanuel's eye for good leaders.

On a personal note, I'd like to thanks all my friends in the UK and in Germany, without whom... God knows where I'd be. To the Smashers and the Waybacks, can't wait to spend more time with you again. To the friends I met here in Munich, thanks for dragging me out of the lab when I needed it, even when I didn't realise. Special thanks in particular to Merve, Hamish, Dima and André - despite our movements I hope to continue these conversations long after we leave Munich.

Finally, and most importantly, thanks to my family - Mary, Barry, Sarah, Paul, Mark, Aasia and Stephen - it's been too long and I can't wait to be home. I love you all.

Priest Ch'ien-Feng addressed his assembly:
"*This Dharma-body has three kinds of sickness and two kinds of light. Can any of you clarify that?*"
Yün-men came forward and said,
"*Why doesn't the fellow inside the herimtage know what's going on outside?*"
Ch'ien-Feng roared with laughter.
"*Your student still has his doubts,*" Yün-men said.
"*What are you thinking of?*" said Ch'ien-Feng.
"*That's for you to clarify,*" said Yün-men.
"*If you're like that,*" Ch'ien-Feng said, "*I'd say you're home free.*"